THESIS FOR THE DEGREE OF DOCTOR OF PHILOSOPHY

In-situ monitoring of laser powder bed fusion applied to defect detection

CLAUDIA SCHWERZ

Department of Industrial and Materials Science
CHALMERS UNIVERSITY OF TECHNOLOGY
Gothenburg, Sweden 2023

In-situ monitoring of laser powder bed fusion applied to defect detection
CLAUDIA SCHWERZ
ISBN 978-91-7905-901-9

© CLAUDIA SCHWERZ, 2023

Doktorsavhandlingar vid Chalmers tekniska högskola
Ny serie nr 5367
ISSN 0346-718X

Department of Industrial and Materials Science
Chalmers University of Technology
SE-412 96 Gothenburg
Sweden
Telephone + 46 (0)31-772 1000

Cover:
A modified optical tomography image showing process by-products being ejected from parts in manufacturing and landing on neighboring parts. More information found in pages 37-38.

Printed by Chalmers Reproservice
Gothenburg, Sweden 2023

In-situ monitoring of laser powder bed fusion applied to defect detection
CLAUDIA SCHWERZ

Department of Industrial and Materials Science
Chalmers University of Technology

ABSTRACT

Additive manufacturing technologies, particularly laser powder bed fusion (LPBF), have received much attention recently due to their numerous advantages over conventional manufacturing methods. However, the use of LPBF is still quite restricted, mainly due to two factors: its typically low productivity, which makes the technology less competitive in applications with moderate to high production volumes, and its limited reliability, particularly relevant for applications where high performance is required from the materials.

The issue of low productivity is addressed in this thesis by adjusting the main LPBF process parameters. An equation for the build rate was formulated based on these parameters, determining their contributions and enabling strategies for build rate maximization. The changes in microstructure and defect populations associated with increasing productivity were determined.

The reliability issue was explored by investigating defect formation, detectability and mitigation, since a major factor compromising reliability and materials' performance is the presence of defects. Internal defects were deliberately created in LPBF-manufactured material to assess their detectability via in-situ monitoring. Two main routes of deliberate defect formation have been identified while preserving defect formation mechanisms; therefore, this thesis can be divided into two parts according to the approach employed to create defects.

Defects are generated systematically if suboptimal process parameters are employed. The types, quantities, and sizes of defects in nickel-based alloy Hastelloy X resulting from varying processing conditions were thoroughly characterized. Analyzing data obtained from in-situ monitoring made it possible to distinguish virtually defect-free material from defective material.

Defects are generated stochastically due to the redeposition of process by-products on the powder bed. With the aid of in-situ monitoring data, the presence of these defects can be inferred from the detection of the process by-products responsible for their formation. The comparison of data obtained in-situ with data obtained through ex-situ material characterization allowed determining how precisely detections corresponded to actual defects. The impact of these defects on the mechanical properties of Hastelloy X was assessed. A couple of in-process mitigation strategies were investigated, and their performances were evaluated.

By establishing means to use LPBF process monitoring to distinguish high-quality from defective material and detect random, unavoidable defects, this thesis enables the prediction of LPBF material quality. It creates conditions necessary for the first-time-right production of defect-free material at increased build rates.

Keywords: Additive manufacturing; powder bed fusion; process monitoring; defect detection; defect mitigation; lack of fusion; pores; spatter; melt pool; nickel-based superalloy; productivity; mechanical properties

PREFACE

The work presented in this doctoral thesis was conducted at the Department of Industrial and Materials Science at Chalmers University of Technology between April 2019 and September 2023 under the supervision of Professor Lars Nyborg. The work was conducted within the framework of the projects MANUELA - Additive Manufacturing using Metal Pilot Line (H2020 Grant No. 820774) and DYNAMIQ (Vinnova 2022-02549) and had the support of the Centre for Additive Manufacturing – Metal (CAM2) – Vinnova and Production Area of Advance, Chalmers.

List of Appended Papers

Paper I **Linking in situ melt pool monitoring to melt pool size distributions and internal flaws in laser powder bed fusion**

Metals 2021, Vol. 11, Page 1856, 11.11 (2021), 1856

C. Schwerz, L. Nyborg

doi.org/10.3390/met11111856

Paper II **Pixel intensity of near-infrared long-exposure images acquired in-situ as a quality control tool in laser powder bed fusion of Ni-base Hastelloy X**

Proceedings of World PM 2022 Congress and Exhibition 2022

C. Schwerz, L. Nyborg

Paper III **A neural network for identification and classification of systematic internal flaws in laser powder bed fusion**

CIRP Journal of Manufacturing Science and Technology, 2022

C. Schwerz, L. Nyborg

doi.org/10.1016/j.cirpj.2022.02.010

Paper IV **Increasing productivity of laser powder bed fusion manufactured Hastelloy X through modification of process parameters**

Journal of Manufacturing Processes, 2022

C. Schwerz, F. Schulz, E. Natesan, L. Nyborg

doi.org/10.1016/j.jmapro.2022.04.013

Paper V **In-situ detection of redeposited spatter and its influence on the formation of internal flaws in laser powder bed fusion**

Additive Manufacturing, 2021

C. Schwerz, A. Raza, X. Lei, L. Nyborg, E. Hryha, H. Wirdelius

doi.org/10.1016/j.addma.2021.102370

Paper VI **In-Situ Detection of Stochastic Spatter-Driven Lack of Fusion: Application of Optical Tomography and Validation Via Ex-Situ X-Ray Computed Tomography**

Additive Manufacturing, 2023

C. Schwerz, B. Bircher, A. Küng, L. Nyborg

doi.org/10.1016/j.addma.2023.103631

Paper VII **Effect of layer thickness on spatters oxidation of Hastelloy X alloy during powder bed fusion-laser beam processing**

Powder Technology, 2023

A. Raza, C. Schwerz, C. Pauzon, L. Nyborg, E. Hryha

doi.org/10.1016/j.powtec.2023.118461

Paper VIII **Mechanical properties of Hastelloy X produced by laser powder bed fusion and affected by spatter redeposition**

Manuscript

C. Schwerz, J. Moverare, V. Sundar, B. Bircher, A. Küng, D. Riabov, L. Nyborg

Paper IX **Surface chemical analysis of spatter particles generated in laser powder bed fusion of Hastelloy X in process atmospheres with high and low oxygen content**

Surface and Interface Analysis, 2023

C. Schwerz, Y. Cao, L. Nyborg

doi.org/10.1002/sia.7202

Paper X **Reduction of the oxygen content in the laser powder bed fusion process atmosphere – effects on stochastic defect formation and mechanical properties of Hastelloy X**

Manuscript

C. Schwerz, J. Moverare, A. Küng, , B. Bircher, D. Riabov, L. Nyborg

Paper XI **Modification of the laser scan pattern in laser powder bed fusion and its effects on stochastic defect formation and mechanical properties**

Manuscript

C. Schwerz, J. Moverare, A. Küng, , B. Bircher, D. Riabov, L. Nyborg

Contribution to the appended papers

Papers I, II, III: I conceptualized, planned, and executed the experimental work and analysis of the results, and drafted the manuscript, which the co-author revised.

Paper IV: I conceptualized, planned, and executed the experimental work and analysis of the results, except for EBSD analysis and tensile testing. Dr. Fiona Schulz planned and performed the EBSD analysis. Dr. Elanghovan Natesan planned and performed the tensile tests. I wrote the manuscript in collaboration with Dr. Fiona Schulz. The remaining co-authors then revised the manuscript.

Paper V: I conceptualized, planned, and executed the experimental work and analysis of the results, except for the SEM and XPS analyses and ultrasonic inspection. Dr. Ahmad Raza conducted the SEM and XPS analysis. Dr. Xiangyu Lei conducted the ultrasonic inspection. I drafted the manuscript, which the co-authors revised.

Papers VI, VIII, X, XI: I conceptualized the work, planned, and executed the experimental work and analysis of the results, except for the XCT and EBSD analyses and mechanical testing. Prof. Johan Moverare planned and performed the mechanical tests. Dr. Benjamin Bircher and Dr. Alain Küng conducted the XCT measurements and data analysis. Dr. Dmitri Riabov performed the EBSD analysis. Vishal Sundar assisted with the fractographic analysis in paper VIII. I drafted the manuscript, which the co-authors revised.

Paper VII: I was responsible for the LPBF manufacturing, planning and execution, and spatter sampling. I analyzed the OT data and revised, together with the remaining co-authors, the manuscript written by Dr. Ahmad Raza.

Paper IX: I conceptualized the work together with Prof. Lars Nyborg. I planned and executed the experimental work and analysis of the results with Prof. Yu Cao. I drafted the manuscript, which the co-authors revised.

CONTENTS

ABSTRACT .... **I**

PREFACE .... **III**

CONTENTS .... **VII**

CHAPTER 1 - INTRODUCTION **1**

1.1 MOTIVATION 1
1.2 OBJECTIVES 2
1.3 SCOPE AND LIMITATIONS 2
1.4 THESIS STRUCTURE 3

CHAPTER 2 - LASER POWDER BED FUSION **5**

2.1 HARDWARE AND WORKING PRINCIPLE 5
2.2 PHYSICAL PRINCIPLE 6
2.3 PROCESS BY-PRODUCTS 7
2.4 PRODUCTIVITY 9

CHAPTER 3 - DEFECTS IN LASER POWDER BED FUSION **11**

3.1 TERMINOLOGY 11
3.2 LITERATURE REVIEW 11
3.3 FRAMEWORK 12
3.4 INFLUENCE OF DEFECTS ON MECHANICAL PROPERTIES 14

CHAPTER 4 - HASTELLOY X **17**

4.1 METALLURGY 17
4.2 APPLICATIONS 17
4.3 LASER POWDER BED FUSION 17

CHAPTER 5 - PROCESS MONITORING **19**

5.1 LITERATURE REVIEW 19
5.2 FRAMEWORK 20

CHAPTER 6 - MATERIALS AND METHODS **23**

6.1 MATERIAL 23
6.2 LASER POWDER BED FUSION SYSTEM AND MANUFACTURING 23
6.3 PROCESS MONITORING: DATA ACQUISITION AND ANALYSIS 24
6.4 EX-SITU ANALYTICAL TECHNIQUES 28

CHAPTER 7 - SUMMARY OF RESULTS **31**

7.1 SYSTEMATIC DEFECTS 31
7.2 PRODUCTIVITY ENHANCEMENT IN THE DEFECT-FREE ZONE 35
7.3 STOCHASTIC DEFECTS 37

CHAPTER 8 - CONCLUSIONS **49**

CHAPTER 9 - FUTURE WORK **51**

REFERENCES **53**

CHAPTER 1
INTRODUCTION

1.1 Motivation

Additive manufacturing (AM), a collection of production technologies, follows a bottom-up strategy for creating products. Contrasting to traditional subtractive manufacturing techniques, which rely on material removal to shape cast or forged material blocks into finished products, fabrication is accomplished layer by layer.

AM has a high transformative potential and impact on the manufacturing landscape due to its numerous advantages over traditional manufacturing methods. One of these advantages is its design freedom, which enables the production of geometrically complex structures that would be impractical through traditional manufacturing technologies. The expanded design flexibility also brings possibilities to reduce the amount of material needed to produce a component, which is particularly relevant to sectors such as aerospace and automotive, where lighter structures translate into less fuel consumption, apart from reduced material and cost. Furthermore, the amount of waste generated in AM is reduced compared to traditional methods due to the capability of producing near-net-shape parts and the possibility of on-demand manufacturing that minimizes the number of unsold products. Additional potentialities of AM are the reduction or elimination of joining processes achieved by producing components in fewer steps and the reduction of support components (e.g., molds and cutting tools) required in manufacturing.

However, for these technologies to be fully utilized from a societal perspective, additive manufacturing must apply to a wider range of industrial segments and goods while upholding quality standards. Two of the main issues hindering the widespread adoption of AM are its limited reliability, a factor particularly relevant for components with high added value and stringent requirements, and its low productivity, particularly relevant for components with a higher production volume.

Although no manufacturing method can achieve defect-free parts, traditional manufacturing processes have attained a level of maturity where the mechanisms leading to defects are well-understood. Robust defect detection protocols and effective mitigation strategies have been meticulously devised, tested, and widely adopted. Furthermore, specific tolerance thresholds for defects have been defined for various applications. Quality control processes must be implemented similarly in AM. Since AM technologies are relatively new compared to conventional manufacturing techniques, some steps toward implementing components produced through this route are still absent. Even though many defect formation mechanisms have been elucidated, development in defect detection and mitigation are still incipient. Fortunately, the process's layer-by-layer nature entails multiple reprocessing of any material volume unit, thus favoring a unique opportunity to mitigate defects in the process. The in-process defect mitigation is achievable once the capability of monitoring systems to detect defects during the manufacturing process can be demonstrated, and suitable corrective actions are known and can be implemented by taking advantage of the subsequent layer in the manufacturing process to heal the defect.

The current industrial practice for quality control consists of post-manufacturing inspection, which might not always apply to AM components apart from not enabling corrective actions. In particular, inspecting geometrically complex components can demand prohibitive amounts of time and resources or even be impossible due to technical challenges. On the other hand, a well-calibrated and validated in-situ monitoring and control system has the potential to detect defects regardless of part geometry and allow the implementation of corrective actions.

1.2 Objectives

Between April 2019 and March 2023, this thesis was conducted within the framework of the project MANUELA (H2020 Grant No. 820774). MANUELA aimed to develop a metal additive manufacturing pilot line service covering the entire AM development cycle, including simulation, robust manufacturing, online process control, real-time feedback, characterization, post-processing and AM qualification protocols [1]. This thesis addresses quality control through process monitoring focused on detecting internal defects and aims to aid in overcoming the currently limited reliability in the laser powder bed fusion process. The issue of low productivity of LPBF is addressed along with its interplay with defect formation. The vision is surmounting the limited capability of right-first-time production by implementing closed-loop control, i.e., automatic detection and mitigation of defects, and enabling production at high build rates without compromising quality.

The research questions (RQ) formulated from the aims of this thesis are:

- RQ1: How can the available monitoring systems be utilized to detect and quantify internal defects in metal components produced via laser powder bed fusion?
- RQ2: Can the productivity of LPBF be increased without compromising the material's quality?
- RQ3: What is the impact of the defects detected on the mechanical properties of Hastelloy X?
- RQ4: Can the defects detected in LPBF be mitigated in-process?

Table 1: Research questions addressed and type of defect investigated in each of the appended papers.

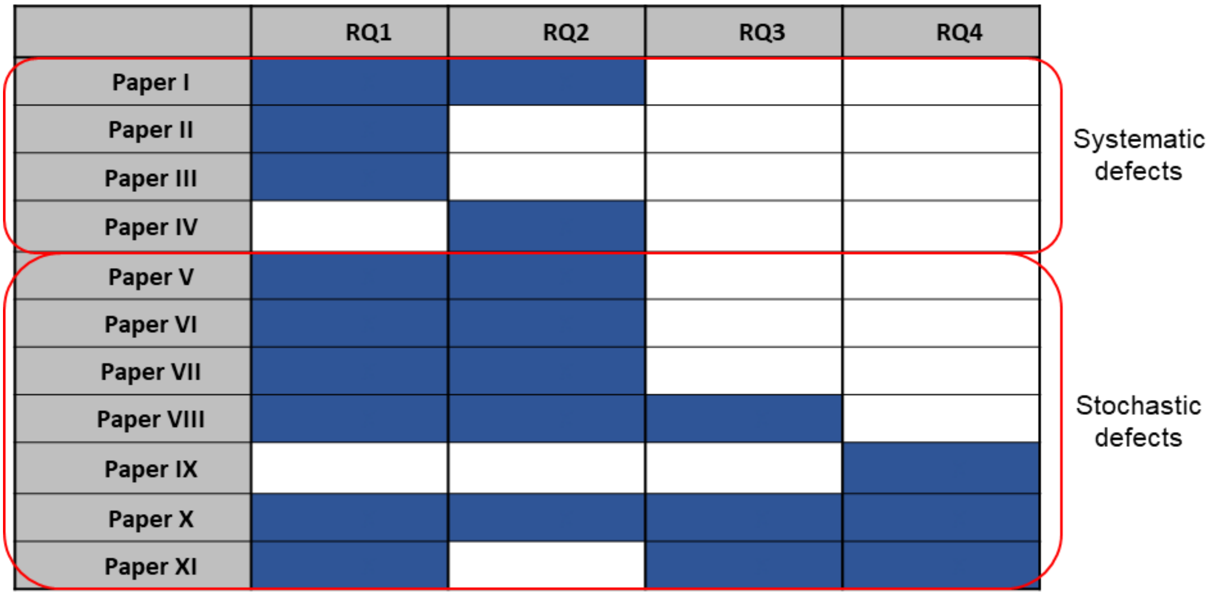

	RQ1	RQ2	RQ3	RQ4	
Paper I	■	■			Systematic defects
Paper II	■				
Paper III	■				
Paper IV		■			
Paper V	■	■			Stochastic defects
Paper VI	■	■			
Paper VII	■	■			
Paper VIII	■	■	■		
Paper IX				■	
Paper X	■	■	■	■	
Paper XI	■		■	■	

1.3 Scope and limitations

The definition of *defects* can be broad and encompass aspects such as geometrical deviations and surface roughness. Evaluating these aspects would require an appraisal of design aspects, additional process parameters, post-processing routes, and in-depth studies of the thermal history. As these factors largely widen the scope, this thesis focuses solely on internal defects, specifically lack of fusion, porosity, and cracks.

The material investigated in this thesis is the nickel-based superalloy Hastelloy X, selected due to project constrains, its favorable printability compared to other superalloys[2] and the importance of defect avoidance in its typical applications. Since Hastelloy X is a single-phase alloy and is not particularly prone to metallurgical cracking, factors external to the alloy that contribute to defect formation can be more readily isolated, thus favoring the detection and control of deliberately created defects. While there have been reports in the literature of Hastelloy X being susceptible to cracking in laser powder bed fusion (LPBF)[3, 4], this issue has not been observed in the present study.

This thesis focuses on characterizing and detecting internal defects in the material, with microstructural characterization having a limited scope. Design considerations and post-processing methods, including surface and heat treatment, are beyond the scope of this study, and the assessment of surface defects is not included.

Effective strategies for mitigating defects are crucial for establishing a closed-loop control system. While several strategies have been examined, this work is not exhaustive and requires further development.

1.4 Thesis structure

This dissertation is structured as a compilation thesis, in which a theoretical background and brief contribution statements are introduced to contextualize the results of the appended papers, which are summarized in the body of the thesis.

This thesis is structured in nine chapters: the present introductory chapter, which aims to motivate and contextualize the research presented here, outline the research questions addressed and structure the thesis. The following chapters (2-5) are divided into relevant topics for understanding this thesis. Each chapter includes an overview of its topic, a literature review, and how this topic is addressed in this thesis. More specifically, which concepts are used or challenged, what assumptions are made, what limitations are present, and what is the added value brought by this thesis.

Chapter 6 describes the experimental procedures. Chapter 7 summarizes the appended papers. Finally, conclusions and suggestions for future work are presented in chapters 8 and 9, respectively.

CHAPTER 2

LASER POWDER BED FUSION

Metal additive manufacturing technologies melt metallic materials in powder, wire, or sheet form with the assistance of an energy source in a layer-by-layer fashion to create dense parts[5]. Metal AM technologies can be divided into broader categories: directed energy deposition, in which energy is used to fuse materials as they are being deposited; powder bed fusion, in which thermal energy selectively fuses regions of thin powder layers spread on the build area[6]; and other technologies, such as material jetting, binder jetting and sheet lamination[7]. Powder bed processes are distinguished by the energy source, electron beam or laser[8]. This thesis is dedicated to studying powder bed metal additive manufacturing employing laser as the energy source, that is, laser powder bed fusion (LPBF).

2.1 Hardware and working principle

The main steps in LPBF manufacturing are[7]:

(1) creation of a 3D representation of the component's geometry;

(2) preparation of the build, which includes the positioning of the part in the build envelope, adding support structures where necessary, and setting up the LPBF machine;

(3) the manufacturing process, performed by spreading a thin powder layer on a build platform and selectively melting according to the part geometry on that layer; lowering the build platform and repeating the process until the part is completed;

(4) post-processing steps, which include cutting the manufactured part from the platform, removing support structures, and performing heat and surface treatments.

Figure 1 is a schematic of the hardware used in laser powder bed fusion, including the monitoring systems used in this thesis, which will be explained in detail in Section 6.3 . The equipment comprises a powder dispenser lifted at each layer to supply powder to the recoater for application on the build platform. The recoater carries excess powder to the powder collector. The laser source, typically a ytterbium fiber laser, is installed outside the build chamber. The laser beam passes through an optical system, is focused with an F-theta lens, and enters the build chamber to expose the powder bed regions that match the geometric model in each layer.

Each laser source has a maximum nominal power, but the laser power P used during exposure is a user-defined process parameter. During exposure, the laser travels at a velocity (or scan speed) v to completely scan the region described by the 3D model in that layer following a predetermined pattern (hatch pattern), where two adjacent tracks are separated by a hatch distance h. On the insert of Figure 1 is a schematic of the stripe pattern, one of the most common laser exposure patterns. The stripe orientation is usually altered between layers by a 67º shift to maximize randomization [9]. The build platform is lowered, the powder dispenser is lifted, the recoater spreads a new powder layer of thickness t, and the process is repeated. The entire procedure is carried out in an inert gas environment, maintained by a gas flow entering the build chamber through the gas inlet.

Special process parameters can be assigned to particular regions of the part. The laser can scan the part boundaries on each layer based on predefined contour parameters, and sections on which no additional layers will be deposited can be assigned a set of *upskin* parameters that contribute to higher surface quality. Overhangs, regions not directly supported by preceding layers or the build plate, can be exposed by *downskin* parameters.

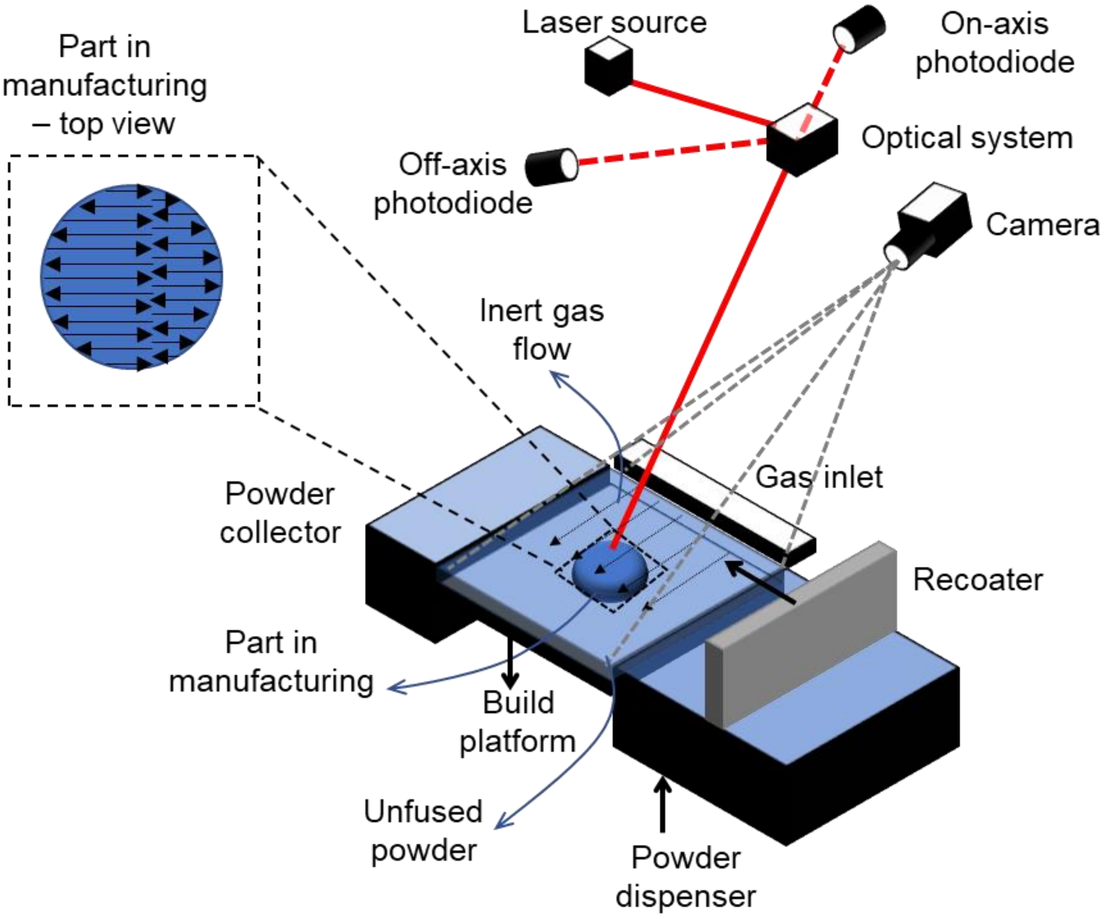
Part in manufacturing – top view
Laser source
On-axis photodiode
Optical system
Off-axis photodiode
Camera
Inert gas flow
Gas inlet
Powder collector
Recoater
Part in manufacturing
Build platform
Unfused powder
Powder dispenser

Figure 1: Schematic laser powder bed fusion hardware with the monitoring systems utilized in this thesis. The insert illustrates the top view of a part in manufacturing and schematizes the laser scan vectors following a stripe exposure pattern.

2.2 Physical principle

During their interaction with the laser beam, the thin layer of feedstock powder and the substrate are fused, forming a pool of molten material. The form and size of melt pools vary depending on the acting heat transfer mechanism. In conduction fusion, the energy is deposited on the piece's surface and transferred to its interior by conduction[10], resulting in melt pools with semicircular cross-sections (Figure 2A). As lasers are used as the energy source, high energy densities are attainable[10], causing some alloying elements to evaporate. Multiple laser reflections occur in the vapor cavity, allowing for higher energy absorption[11] and the formation of a deeper melt pool (Figure 2B). The process is sustained by the competing vapor pressure, which acts to keep the keyhole open, and the pressure from gravitational forces and surface tension, which act to shut the keyhole[12]. The fluid flow in the melt pools is driven by Marangoni convection, wherein the temperature variation in the melt pool produces a spatial gradient of surface tension[11].

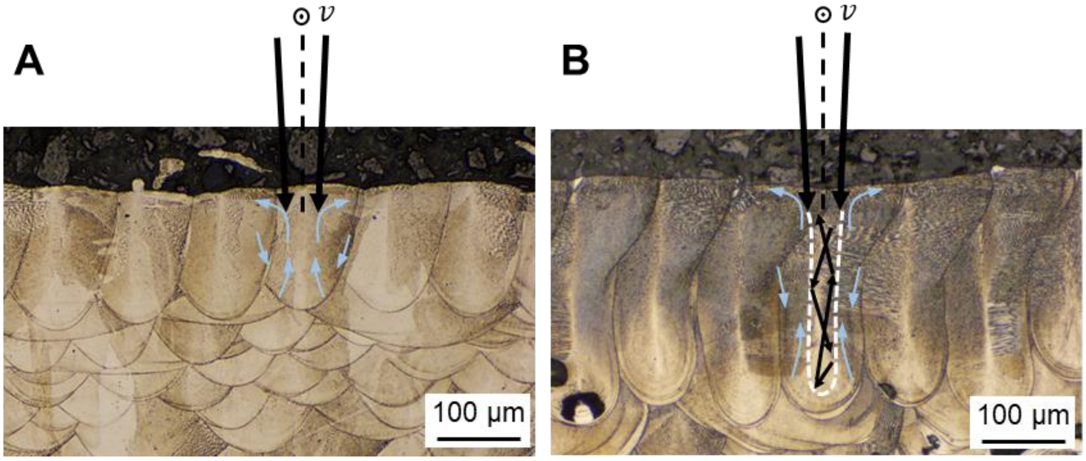

Figure 2: Scheme of fluid flow overlapped to micrographs of melt pools generated in the conduction (A) and keyhole (B) regimes. The laser beam and its travel directions are represented in black. In (B), the vapor cavity is represented with a white dashed line, based on the observations documented in the literature [13].

2.3 Process by-products

Spatters are unavoidable LPBF process by-products that promote defect formation and are formed through several mechanisms schematized in Figure 3. Spatters can consist of (**a**) ejections of molten material from the melt pool due to recoil pressure [14, 15], typically with size of 25 – 100 µm [16]. If the ejecta collide and merge (**b**), even larger spatter particles are formed [16]. Particles entrained by the low-pressure zone created by the vapor jet may interact with the laser beam and be ejected as hot spatters (**c**) [16] or coalesce and be subsequently melted [17], resulting in sizeable incandescent ejecta (**d**). The suddenly unstable interaction between the laser and the part that occurs upon contact with a pre-existing large defect can also cause the formation of hot spatter (**e**)[18]. Cold spatters consist of particles initially present on the powder bed that are scattered by the impact of metallic vapor (**f**)[14] or entrained by the low-pressure zone, then ejected prior to interaction with the laser beam (**g**)[16].

As a result of their formation mechanisms, spatters can be significantly larger than the particles in the powder feedstock [19], as illustrated in Figure 4, and contain relatively thick surface oxides [20]. When redeposited on the powder bed, spatters represent a local increase in powder layer thickness that can hinder the complete melting of the powder layer [21] and attenuate the laser beam [22]. Their surface oxidation represents a local change in the chemistry of the powder bed, which induces contamination and defect formation [23] [24] by modifying the melt pool dynamics [25]. These disturbances potentially result in insufficient binding, i.e., in internal defects [24].

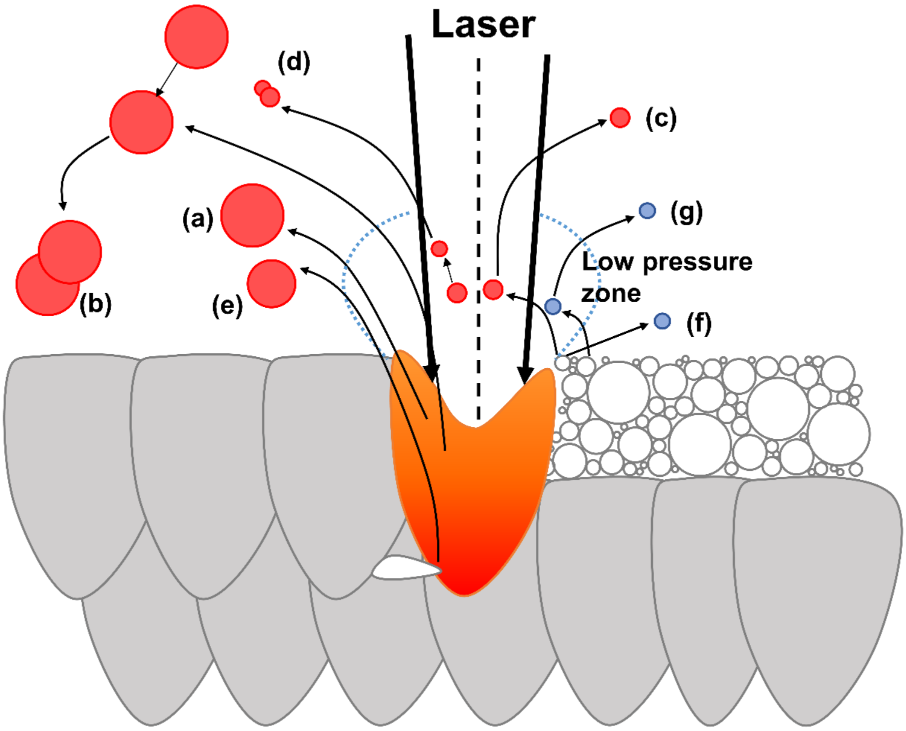
Laser
(a)
(b)
(c)
(d)
(e)
(f)
(g)
Low pressure zone

Figure 3: Scheme of spatter formation mechanisms. Spatters can consist of ejections from the melt pool (a), which can collide and merge (b). The ejection from the melt pool is intensified if the laser interacts with a pre-existing defect (e). Scattered feedstock powder particles can also be considered spatter and are differentiated by being directly scattered (f), scattered after being entrained in the low-pressure zone (g), ejected after interacting with the laser beam (c), or coalescing with another particle (d).

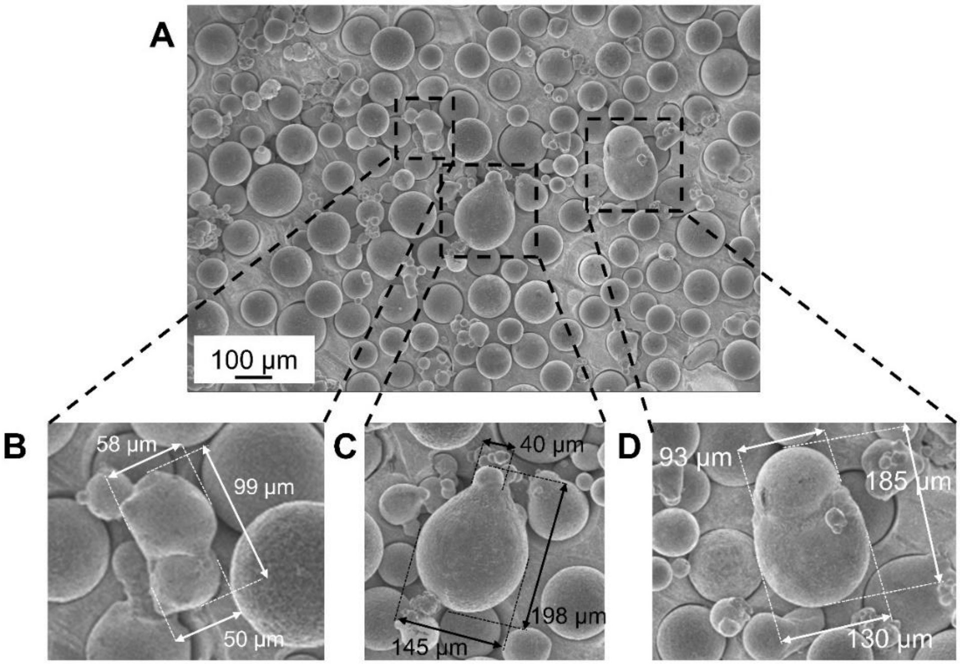
A
100 µm
B
58 µm
99 µm
50 µm
C
40 µm
198 µm
145 µm
D
93 µm
185 µm
130 µm

Figure 4: Morphology of spatter particles. A representative sample is shown in A. Some oversized agglomerates in this sample are highlighted and measured in B, C and D. From **Paper V**[26].

2.4 Productivity

The limited build rates of laser powder bed fusion are a major obstacle to its broad use as an industrial manufacturing technology [27] [28] [29]. This reduced efficiency results in higher costs, rendering the technology less competitive across various industry sectors [30]. As a consequence, its usage remains predominantly confined to high-end applications characterized by low production volumes, where the associated elevated expenses are tolerable [31]. To tackle this challenge, researchers have explored diverse strategies, which can be categorized into two main groups: hardware modifications and process parameter adjustments. Hardware-focused approaches encompass the incorporation of multiple laser sources [30] or higher-power laser sources [32] [33] that facilitate the rapid processing of larger material volumes. However, this aspect of productivity enhancement is beyond the scope of this thesis. On the other hand, altering process parameters is an immediately accessible alternative for improving productivity [27] [34] and can be used to boost the production potential of any LPBF system. It is essential, though, to exercise caution when implementing this approach, ensuring that the pursuit of enhanced productivity does not compromise material quality by inadvertently increasing defect formation.

CHAPTER 3
DEFECTS IN LASER POWDER BED FUSION

3.1 Terminology

According to the Glossary of Metallurgical and Metalworking Terms in the ASM Metals Handbook [35], the term *defect* is defined as:

> *" (1) A discontinuity whose size, shape, orientation, or location makes it detrimental to the useful service of the part in which it occurs. (2) A discontinuity or discontinuities which by nature or accumulated effect (for example, total crack length) render a part or product unable to meet minimum applicable acceptance standards or specifications. This term designates rejectability."*

While the term *discontinuity* has the following definition [35]:

> *"(1) Any interruption in the normal physical structure or configuration of a part, such as cracks, laps, seams, inclusions, or porosity. A discontinuity may or may not affect the utility of the part. (2) An interruption of the typical structure of a weldment, such as a lack of homogeneity in the mechanical, metallurgical, or physical characteristics of the material or weldment. A discontinuity is not necessarily a defect."*

Despite these definitions, the metal additive manufacturing community has widely replaced the term *discontinuity* with *defect*. Also, *defect* has been used as an umbrella term for discontinuities and undesirable characteristics in additively manufactured material. In this context, defects can refer to geometrical deviations, residual stresses, microstructural inhomogeneities and surface roughness [36].

Strictly, this thesis addresses *discontinuities* in LPBF. However, due to the convention in the metal AM community, the term *defect* is consistently adopted, even though this thesis does not aim to provide any assessment on specific acceptance criteria and aims rather to be as generic as possible. In papers I-V, the term *flaw*[1*] is used instead, aiming for better theoretical correctness. In papers VI-X, the most widely used term, *defect*, was adopted.

3.2 Literature review

As stated in Section 2.1, keyhole and conduction are the possible fusion modes upon the interaction of a laser beam with metallic materials. In keyhole fusion, the deep and narrow vapor cavity formed permits more efficient energy use due to the multiple reflections of the laser in this cavity [13]. However, if keyhole fusion is uncontrolled, an incomplete collapse of the vapor cavity may occur, leaving voids consisting of entrapped vapor [37], i.e., keyhole porosity. In the conduction regime, the smaller melt pools facilitate the formation of lack of fusion defects, which derive from the insufficient overlap of adjacent melt pools [38]. In both fusion regimes, spherical and relatively small pores, denominated residual gas pores, are always expected in the as-built material. These pores form due to entrapped gas in the feedstock powder [39] and the decrease in the solubility of gas-forming elements present in the feedstock powder upon solidification [40] [41].

[1*] Defined as "*A nonspecific term often used to imply a cracklike discontinuity*" [35].

3.3 Framework

The main objective of the thesis is to detect internal defects via in-situ monitoring of LPBF. There are two main issues to consider:

- Deliberately creating defects to enable their investigation. While defects will be formed organically, their prevalence may be too low to allow for a meaningful study or would require the examination of a prohibitively large volume of material and data.
- Doing so in a manner that is representative of defects in a real manufacturing scenario. Introducing unrealistic defects artificially by means that do not correspond to actual defect formation mechanisms to assess the response registered by the monitoring systems is not considered meaningful, as such a procedure may produce misleading data on the flagging of anomalies.

Thus, a meaningful, manageable study relies on augmenting defects while preserving their generation mechanisms. Considering these factors, two ways of deliberately generating defects while preserving their generation mechanisms have been found. In this thesis, the classification is based on the incidence and distribution of defects, i.e., if they are created systematically or stochastically. This choice is made since the primary aim of this work, the use of monitoring systems for defect detection, depends on the deliberate creation of defects in a controlled and representative manner. A similar classification system has been utilized in the review article by Snow et al. [40]. The manner by which defects are created affects their distribution, size, and type, requiring distinct approaches for their detection and resulting in distinct impacts on the material performance.

a. Systematic defects

Defects are systematically created in LPBF if inadequate combinations of process parameters are selected for manufacturing. Systematic defects can consist of keyhole porosity, gas porosity, and lack of fusion, and can occur at diverse degrees of severity, as illustrated in Figure 5. Such defects are uniformly distributed throughout the material.

Most literature on defects in LPBF addresses systematic defects, as they arise during process optimization, one of the first stages in the qualification of a new material or machine. Early research work in the field aimed chiefly at maximizing densification, i.e., minimizing the volume fraction of defects. In this context, the volume fraction of systematic defects was used as the main quality metric of LPBF material, often documenting the predominant defect type encountered: pores coupled to materials manufactured with higher energy inputs, or lack of fusion, coupled to lower energy inputs.

Historically, volumetric energy density (VED, calculated as the ratio between laser power and the product laser scan speed, hatch spacing and nominal layer thickness) was used to describe the energy input. For some years, the bulk of scientific production in this area has attempted to correlate the defect content to VED. However, it has been demonstrated that the VED metric does not adequately predict the defect content [42] [43] [38]. For the material and process in this thesis, for example, all categories of systematic defects can be obtained at a fixed value of VED, as illustrated in Figure 6. For these reasons, the concept of VED is avoided in this thesis and appended papers.

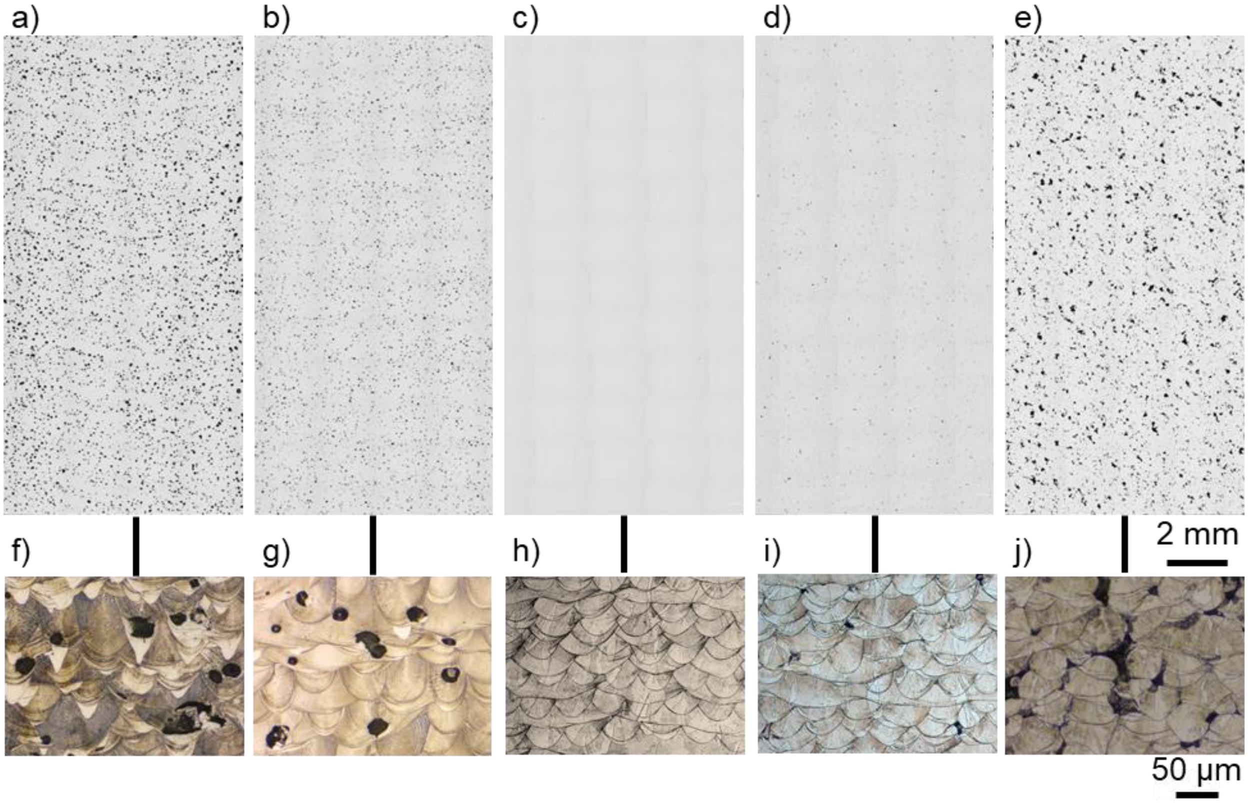
a)
b)
c)
d)
e)
f)
g)
h)
i)
j)
2 mm
50 µm

Figure 5: Cross-sections of samples containing systematic defects. (a) and (b) show systematic keyhole porosity with different degrees of severity (detailed in (f) and (g)). (c) and (h) show a sample virtually free from defects, in which only gas porosity has been identified. (d) and (e) show systematic lack of fusion with different degrees of severity (in detail in (i) and (j), respectively). Adapted from **Paper III**[44].

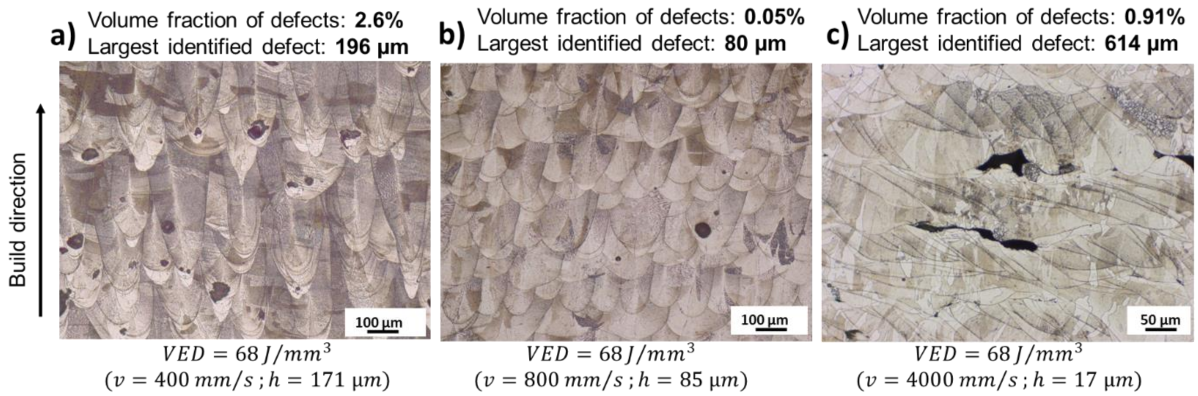
a) Volume fraction of defects: 2.6%
Largest identified defect: 196 µm
b) Volume fraction of defects: 0.05%
Largest identified defect: 80 µm
c) Volume fraction of defects: 0.91%
Largest identified defect: 614 µm
Build direction
100 µm
100 µm
50 µm
$VED = 68\,J/mm^3$
$(v = 400\,mm/s\,; h = 171\,\mu m)$
$VED = 68\,J/mm^3$
$(v = 800\,mm/s\,; h = 85\,\mu m)$
$VED = 68\,J/mm^3$
$(v = 4000\,mm/s\,; h = 17\,\mu m)$

Figure 6: Micrographs of Hastelloy X manufactured via LPBF at a fixed volumetric energy density of 68 J/mm^3. Varying defect populations are obtained at fixed VED: a) keyhole porosity at a volumetric fraction of 2.6%; b) residual porosity at a fraction of 0.05%; c) lack of fusion at a fraction of 0.91%. The laser scan speed v and hatch spacing h used are indicated. Laser power of 370 W and a nominal layer thickness of 80 µm were used in all cases.

b. Stochastic defects

Internal defects can form stochastically in LPBF due to, e.g., irregularities in the powder bed and process by-products [40]. Differently from systematic defects, the occurrence and distribution of stochastic defects can, in principle, not be anticipated, as their formation is not driven (albeit can be influenced) by user-defined parameters[14 45 46]. The distribution of stochastic defects is irregular, as illustrated in Figure 7, which shows cross-sections of specimens manufactured at constant processing conditions. Linearly distributed defects, such as the ones illustrated in Figure 7c, indicate powder bed anomalies or recoating faults. Multiple (Figure 7a,c) or single (Figure 7b,d) stochastic defects may be present in a specimen and can coexist with systematic defects (Figure 7c,d). In this thesis, the focus is given to stochastic defects provoked by process by-products, more specifically spatter.

As described in Section 2.3, spatters are LPBF process by-products whose formation is inherent to the process and have been reported as one of the primary sources of stochastic defects [22 40]. Due to their varied formation mechanisms, spatters can have different sizes, morphologies and temperatures upon ejection, which affects their detectability through in-situ monitoring.

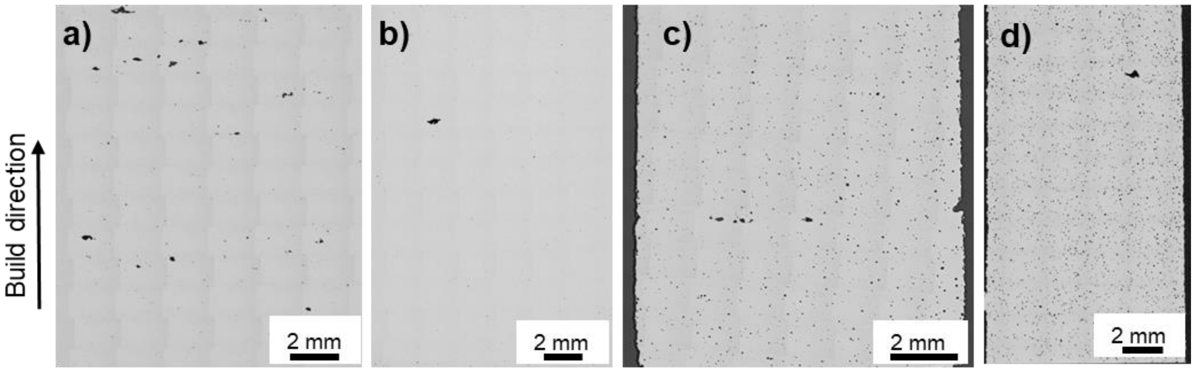

Figure 7: Cross-sections of samples containing stochastic defects. Multiple (a) and single (b) stochastic defects occurring in otherwise virtually defect-free specimens. Multiple, linearly distributed stochastic defects (c) and a single stochastic defect occurring with systematic defects.

A. Influence of defects on mechanical properties

Defects have a limited influence on the tensile properties but can be detrimental in large proportions by reducing the load-bearing cross-sectional area [47]. On the other hand, defects significantly influence fatigue properties, as their presence means the initial phases of fatigue damage are bypassed [48]. Defects act as stress raisers [49], and, as such, factors such as their morphology, size [50] and position [51 52] determine their criticality. Partly due to the many sources of internal defects in AM materials, the variability in fatigue properties [49 53 54] is a widely reported issue that hinders the use of the technologies in critical load-bearing applications [55].

Apart from defects, other reasons for the scatter in fatigue properties of AM materials are surface finish, microstructure, and residual stresses [55]. The most critical factor has been reported to be the surface finish [55 56], as the surface of as-printed materials is generally rougher than traditionally manufactured materials and acts as multiple stress concentrators. The surface roughness can be managed through different post-processing routes, and surface-treated AM materials have been reported to present superior fatigue properties than their conventionally manufactured counterparts, thanks to their finer microstructure [55].

The fine microstructure acts as an effective obstacle for dislocation motion and promotes strengthening of the material, improving fatigue performance, especially at longer lives [51]. Indeed, some studies have reported a dominant effect of the microstructure and limited influence of defects in the fatigue performance of LPBF material [57 58 50]. Moreover, processing strategies that increase the cooling rate during solidification have been proposed to improve fatigue resistance [58].

Surface treatment combined with hot isostatic pressing (HIP) has been reported to improve the fatigue resistance of LPBF material [59], as HIP can eliminate defects not open to the surface. On the other hand, scatter in fatigue properties has also been reported to persist even with the improvements given by the combined post-processing steps [60], as HIP promotes two conflicting effects to the fatigue performance: eliminating internal defects and coarsening the microstructure.

CHAPTER 4
HASTELLOY X

4.1 Metallurgy

Hastelloy X is a nickel-chromium–iron-molybdenum alloy, also referred to as a superalloy due to its outstanding resistance to mechanical and chemical degradation at high temperatures over extended periods of time [61]. Nickel is the primary alloying element of most heat-resistant superalloys and forms an austenitic structure that is more formable than ferritic structures of equivalent strength. The addition of chromium increases the strength and oxidation resistance at elevated temperatures, while iron reduces the susceptibility to internal oxidation [62], provides solid solution strengthening and enables cost reduction. Elements with large atomic radii, such as molybdenum and tungsten, contribute to high-temperature creep strength, as strength is diffusion-dependent in elevated temperatures [62]. Unlike other nickel-based superalloys, Hastelloy X is not enriched with titanium and niobium, elements that form the strengthening phases gamma prime and gamma double prime. On the other hand, Hastelloy X is prone to carbide formation, particularly during heat treatment or service in high temperatures, improving the creep properties due to the preferred formation site at grain boundaries [61]. Therefore, the primary strengthening mechanism in Hastelloy X is solid solution strengthening of the face-centered cubic (FCC) matrix, with a minor influence of carbide precipitation [63].

4.2 Applications

Hastelloy X is used in petrochemical applications due to its high resistance to stress-corrosion cracking, in the combustion zone of gas turbine engines due to its exceptional combination of oxidation resistance and high-temperature strength, and in industrial furnaces due to its resistance to oxidizing, reducing and neutral atmospheres [64]. Considering that defects may compromise both corrosion properties and mechanical performance required from Hastelloy X, the capability of manufacturing virtually defect-free material is critical. For LPBF manufacturing, this capability can be achieved with the aid of monitoring systems in defect detection and mitigation, thus motivating this study and material selection.

4.3 Laser powder bed fusion

Matrix-strengthened nickel-base alloy Hastelloy X is regarded as having good weldability [64], meaning it is not particularly susceptible to metallurgical cracking. The AM community is, however, not unanimous concerning crack formation during LPBF manufacturing of Hastelloy X. This issue has been reported and addressed in numerous studies [65] [3] [66] [4], whereas others have observed crack-free material [67] [68] [69]. This inconsistency is likely due to minor compositional changes [3], known to influence cracking susceptibility [70]. Throughout the work performed in this thesis, a significant part of the process parameter space was investigated, and no cracks were observed in any processing condition. This suggests that the specific chemical compositions of the feedstock powders used in this study are robust to cracking mechanisms. As no cracks were observed, the internal defects addressed in this thesis are limited to lack of fusion and pores.

The typical microstructure of LPBF Hastelloy X can be seen in Figure 8, where its hierarchical organization [71] is depicted. The temperature gradient promotes epitaxial grain growth in the build direction, thus forming the columnar grains visible in Figure 8A across melt pool boundaries. Within the grains, cellular microstructure consisting of high-density dislocation walls [72] is observed (Figure 8C). The microstructure of LPBF Hastelloy X can vary significantly based on the processing conditions, as shown in Figure 9, depicting three different cross-sections of materials manufactured with distinct processing parameters. Anisotropy is typically observed in the as-printed state due to the directional heat transfer and solidification and can also be seen in Figure 9.

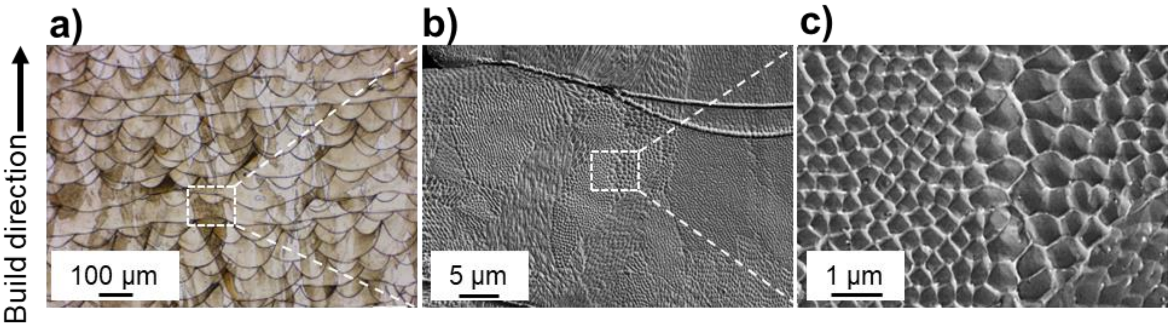

Figure 8: Hierarchical microstructure of as-built Hastelloy X. (a) In the microstructure observed at relatively low magnification through light optical microscopy, columnar grains oriented along the build direction and melt pool boundaries are visible. (b) Through SEM imaging, the cellular microstructure is visible within grains. The well-defined lines are melt pool boundaries. (c) Detail on cell structure. From **Paper IV**[73].

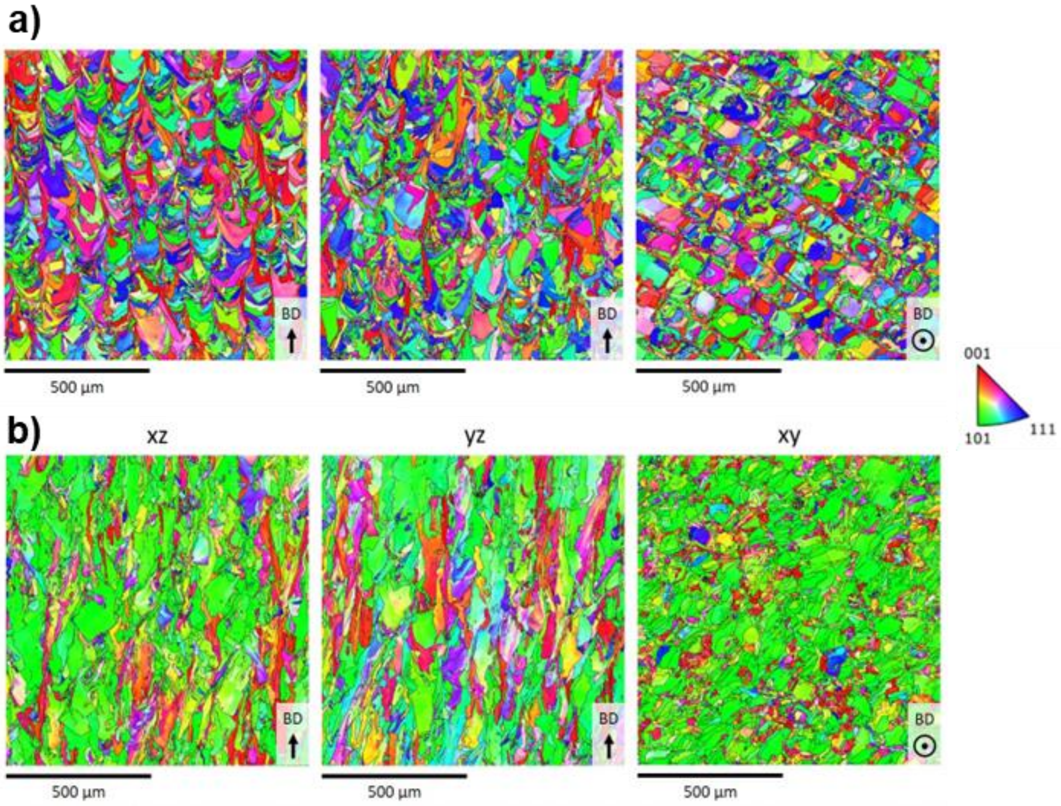

Figure 9: EBSD orientation maps showing the microstructure of Hastelloy X manufactured with different processing conditions in three planes. The build direction (BD) is indicated. Adapted from **Paper IV**[73].

CHAPTER 5
PROCESS MONITORING

Beyond enabling the tracking of the manufacturing process, process monitoring can be used as a quality assurance tool. Process monitoring data allows alternative observations of the process, depending on the setups employed, including the detector, acquisition rate, and acquisition areas. With that, different process signatures are observed, and once patterns are established, anomalies can be distinguished. These process anomalies may be coupled to defects in the material, in which case a timely detection is desirable. Monitoring data can also be used for documentation, for example, in the aerospace and medical industries, where production data must be available for years in the future for traceability purposes. The capabilities of various monitoring setups in various applications, including defect detection, have been investigated in the literature. As this area of knowledge is relatively novel, a brief literature review will be presented in the next section.

5.1 Literature review

Monitoring systems can be distinguished by the spectral range of the signal acquired and by the acquisition system employed, which can comprise regions of distinct extensions and generate different outputs at varying rates. The selection of acquisition system and spectral ranges determine the process phenomena and deviations that can be captured, as well as the attainable data processing speed. Thus, different monitoring system setups have different best application areas and varying capabilities of being implemented in practice as quality assurance tools.

One of the most common setups for detecting LPBF process anomalies includes a camera that acquires signal in the visible spectrum across the entire build area layerwise, after recoating and laser exposure. This setup is the baseline of most commercially available process monitoring solutions due to its simplicity and utility. It allows the identification of recoating anomalies, such as recoater streaking and incomplete spreading, and geometrical anomalies, such as part swelling and warping. Beyond pure observation of anomalies, machine learning approaches have been employed to differentiate powder spreading issues [74], and distinguish irregularities from the desirable, normal operating conditions [74] [75]. Even though internal defects often originate from issues other than inhomogeneities on the powder bed, the capability of this setup for internal defect detection has been investigated [76] [77] [78].

Process monitoring based on the acquisition of infrared emissions using single photodiodes has been typically used to monitor melt pools in LPBF, as the signal is acquired from a small surface area at a time [79]. Some applications identified in the literature are monitoring melt pool intensity [80] and detecting keyhole pores in single tracks [81]. Some studies have applied monitoring with photodiodes to more representative multilayer builds to detect deformations due to thermal stresses and overheating in overhang structures [82] and stochastic defects [83] [84]. However, labor-intensive, time-consuming data processing has been listed as a limitation [83].

Other monitoring systems that collect high-resolution data are based on high-speed cameras and acoustic emissions, which, due to the large amount of data generated, are also often limited to the analysis of single tracks. Machine learning approaches have been applied to classify images acquired through high-speed cameras [85] [86] and acoustic signals [87] into categories based on the quality of single tracks, such as balling, continuous tracks and keyhole porosity.

Acoustic emissions could also be applied to determine the quality of a bulk specimen containing sections manufactured at different sets of process parameters, yielding systematic defects [88].

In-situ X-ray imaging has been used to elucidate the phenomena occurring in the LPBF process. Some of the main investigation areas are melt pool dynamics [89] [90] and spattering [91] [92]. Given the detail required to study these phenomena, data is acquired at high frequency, and the field of view is limited to a few millimeters. Thus, this monitoring solution, like others mentioned, is nowadays mostly applicable to fundamental research, and its integration into commercial LPBF machines would require major adjustments.

Cameras can be used to capture signal from the entire build area and, if employed in conjunction with high-pass filters, can be used for thermal sensing [93]. For example, thermal imaging has been used to identify delamination and spatter [94], and detect internal defects [95]. However, reliable temperature measurements can only be obtained through specific devices, such as pyrometers, which undergo rigorous and careful calibration before being considered temperature measurement devices [96].

5.2 Framework

For a monitoring system to be used for defect detection, it is necessary to calibrate and qualify the detection procedure to ensure a fair correspondence between detections and defects of interest. In traditional non-destructive inspection methods, defects of controlled dimensions are created artificially, and the system is calibrated to generate a distinct signal in those locations. Since in AM the goal is to detect defects while the manufacturing process is ongoing, the method employed in deliberately creating defects becomes an issue to be considered. Void seeding, i.e., adding voids in the CAD model, has been reported in the literature [75] [97] [98] [99]. However, this approach contains limitations as it does not mimic the process of defect formation and, by basing calibration of the system on those voids, fine features usually present in the design of AM parts will be incorrectly flagged as defects. Thus, in this thesis, it is considered that to calibrate the system, the process of intentionally creating defects must preserve the physics of defect formation. In the case of systematic defects, altering the process parameters generates defects. In the case of stochastic defects, defects are sparsely generated due to, e.g., process by-products. To increase the likelihood of defect formation, some strategies reported in the literature are modification of the gas flow [84] and reduction of the gas flow speed [100].

In this thesis, only the EOSTATE suite (EOS GmbH) was used for monitoring aiming at defect detection. The systems in the suite have distinct characteristics, described in Section 6.3 . These characteristics make each system more suitable for different purposes and justify the different extents to which each system is used. In some cases, anomalies related to internal defects are observed in multiple systems, as illustrated in Figure 10, where recoating faults could readily be observed in the PowderBed system from layer N to N+3 (Figure 10a). A delayed response was visible in the optical tomography (OT) system, from layer N+3 to layer N+6 (Figure 10c). The consequences of the recoating faults were a streak of defects observed on the build height corresponding to the faulty layers (Figure 10b).

With the monitoring systems used in this work, it is not typically possible to directly observe internal defects, as is the case, for example, in in-situ X-ray imaging. Only anomalies are typically visible. This thesis aims to generate a better understanding of various anomalies and correlate them to specific types of defects, characterized ex-situ by well-established methods whose measurements are the ground-truth data (i.e., empirical evidence) for defect detection. With that, the goal is to process monitoring data and infer the presence of defects from it.

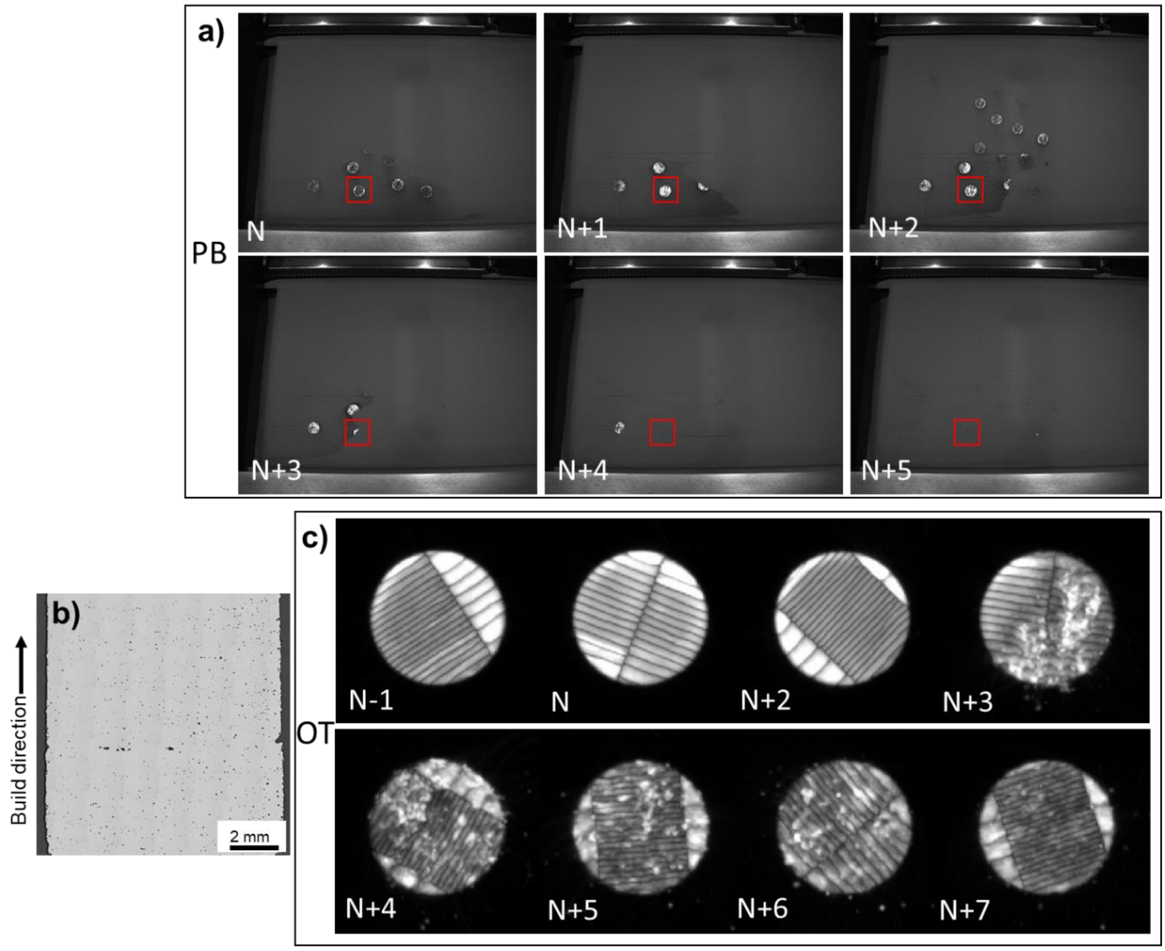
a)
PB
N
N+1
N+2
N+3
N+4
N+5
b)
Build direction
2 mm
c)
OT
N-1
N
N+2
N+3
N+4
N+5
N+6
N+7

Figure 10: Recoating faults in layers N to N+3 are visible in PowderBed (PB) images (a). The faults resulted in a streak of defects in the specimens affected (b) and manifested as anomalies in OT images on layers N+3 to N+6, approximately (c). The position of the specimen represented in (b) is indicated by red squares in (a).

CHAPTER 6
MATERIALS AND METHODS

6.1 Material

The work performed in this thesis used gas atomized Hastelloy X, partly from EOS GmbH, and partly from Höganäs AB. The powder from supplier EOS has particle sizes ranging from 19 µm (d10) and 58 µm (d90), and d50 of 35 µm. A sample of the virgin feedstock powder can be seen in Figure 11. Its nominal chemical composition, as provided by the manufacturer, is presented in Table 2.

Table 2 Nominal composition of the EOS feedstock powder. The minimum and maximum weight percentages of each element are presented.

	Ni	Cr	Fe	Mo	W	Co	C	Si	Mn	S	P	B	Se	Cu	Al	Ti
Min	Bal	20.5	17.0	8.0	0.2	0.5	--	--	--	--	--	--	--	--	--	--
Max		23.0	20.0	10.0	1.0	2.5	0.1	1.0	1.0	0.03	0.04	0.01	0.005	0.5	0.5	0.15

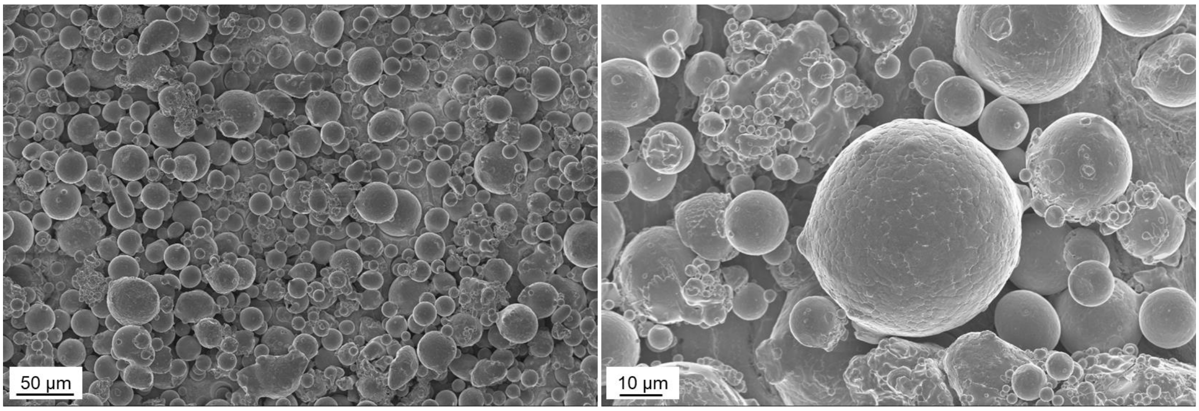

Figure 11: Sample Hastelloy X feedstock powder supplied by EOS GmbH.

6.2 Laser powder bed fusion system and manufacturing

The LPBF manufacturing was performed in an EOS M290 machine (Electro Optical Systems GmbH, Germany), equipped with an ytterbium fiber laser of maximum nominal power of 400 W and a focused beam diameter of 100 µm. The processing atmosphere consisted of argon with a maximum oxygen concentration of 1000 ppm, and further restricted to 50 ppm in parts of Papers IX and X. The inert gas enters the process chamber through a nozzle. For EOS M290, there are two commercially available nozzles: the standard nozzle, in which the gas enters the build chamber through circular channels, and the grid nozzle, which contains rectangular channels arranged in a grid and is constructed to project the gas flow downwards on the row closest to the powder bed. The standard nozzle was used in most of this thesis' work, while the grid nozzle was used in the studies documented in Papers VIII – XI. The nozzle employed might have influenced the distribution of spatter redeposits across the build area.

Throughout the work composing this thesis, relatively simple specimen geometries were used to avoid the incorporation of defects driven by factors such as design and parameters assigned to special areas (*downskin* and *upskin*). To minimize the influence of factors other than the objects of study, the general processing conditions were maintained unaltered as per the machine manufacturer's recommendations or default values, unless explicitly stated otherwise. Examples of such factors are the atmosphere, the chamber's differential pressure, the build platform's preheating temperature, and the scan strategy.

In the studies aiming to investigate systematic defects, precautions were taken to avoid stochastic defects. The specimen dimensions were reduced to prevent the redeposition of spatter formed during exposure of the upstream region of the specimen on the region downstream. The specimens were positioned with a minimum spatial gap of 40 mm and avoiding the region of the build area closest to the gas outlet. The powder dosing was boosted to avoid incomplete spreading of the powder layer. The design did not include geometrically complex features to avoid recoating-related defects.

Conversely, when studying stochastic defects, the source of systematic defects was eliminated, i.e., the process parameters employed were previously optimized and demonstrated to produce only residual porosity as bulk defects in the as-printed condition. To isolate the influence of process by-products on the formation of stochastic defects, the same measures as described above were taken to eliminate other potential sources of stochastic defects.

6.3 Process monitoring: data acquisition and analysis

LPBF manufacturing was monitored using the EOSTATE suite [101], which comprises three monitoring systems. The systems differ based on factors such as sensor type, field of view, acquisition rate and range. The process radiation and the spectral ranges acquired by the EOSTATE sensors are schematized in Figure 12. Yet another important difference among the systems is the amount of data generated which poses varying challenges in terms of storage and processing. The data output from the different systems is summarized in Table 3, which includes the size occupied on disk by the data generated from a 500-layer build.

Sample outputs of the three systems, representing the same build layer, where varying processing parameters are applied, can be visualized in Figure 13, Figure 14 and Figure 15. These systems were mainly used for data acquisition; data processing and analysis were mainly performed externally to the systems. In Papers IX and X, the oxygen content in the process atmosphere is controlled and monitored through the ADDvance system (Linde GmbH) and the oxygen sensor built into EOS M290, respectively. Additional process data monitored by default are the laser power, the platform temperature, and the laser exposure duration per layer.

Table 3: Data output from the EOSTATE monitoring systems.

Monitoring system	**Output type**	**Output size**	**Data generated in a small build (500 layers)**
Powder bed (PB)	1280 ×1024 pixel JPEG image	~85 kB	76 MB (pre- and post-recoating)
Optical tomography (OT)	2000 × 2000 pixel TIFF 16-bit image	7.63 MB	7.48 GB (*INT* and *MAX* outputs)
Melt pool monitoring (MPM)	Proprietary file format (.mpm), .h5 file, PNG image	~90 MB	27.72 GB

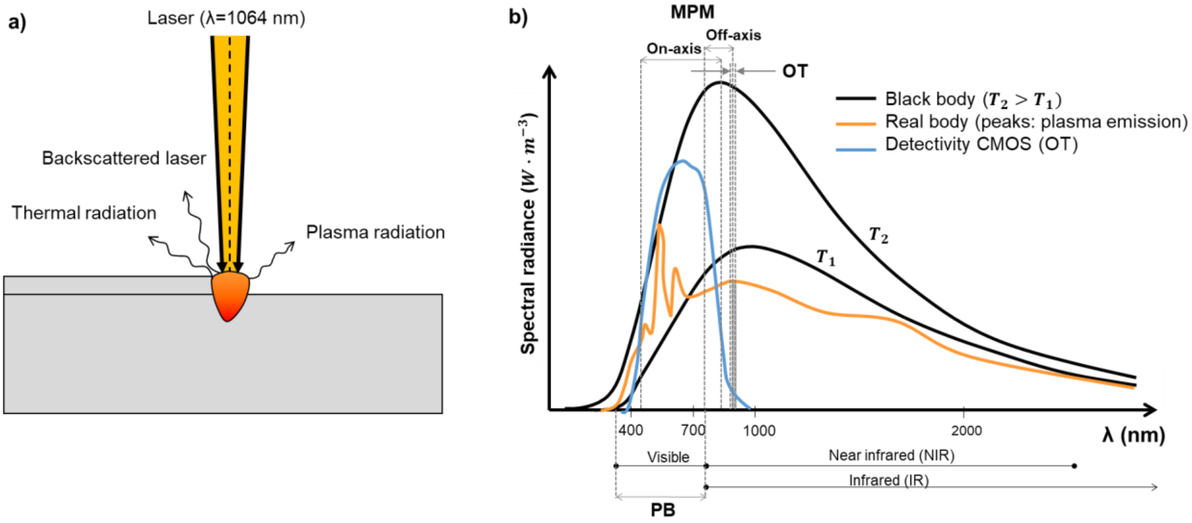
a)
Laser (λ=1064 nm)
Backscattered laser
Thermal radiation
Plasma radiation
b)
MPM
On-axis
Off-axis
OT
Black body ($T_2 > T_1$)
Real body (peaks: plasma emission)
Detectivity CMOS (OT)
Spectral radiance ($W \cdot m^{-3}$)
T_2
T_1
400
700
1000
2000
λ (nm)
Visible
Near infrared (NIR)
Infrared (IR)
PB

Figure 12: (a) Scheme of laser powder bed fusion process radiation. (b) Scheme of emitted radiation and acquisition spectral ranges of the sensors in EOSTATE. Adapted from Zenzinger et al.[102] and EOSTATE training material.

a. Powder bed monitoring

EOSTATE PowderBed (PB) is an optical monitoring system that includes the entire powder bed in the field of view of the charge-coupled device (CCD) camera and outputs two images of the powder bed per layer, one post-exposure and one post-recoating. These outputs are illustrated in Figure 13 A and B, respectively. The image acquired post-exposure can reveal irregularities on the printed surface and the deposition of process by-products on the powder bed, as depicted in the insert of Figure 13 A. The image acquired post-recoating can reveal issues related to recoating, such as streaking (visible in the insert of Figure 13 B) and incomplete powder spreading. Powder packing issues, common in correlation to challenging geometrical features, are also best visualized in PowderBed post-recoating. Part swelling and bulging from the powder bed is visible in this output, manifesting as high-intensity blobs (as in the insert of Figure 13 B), lines or patches.

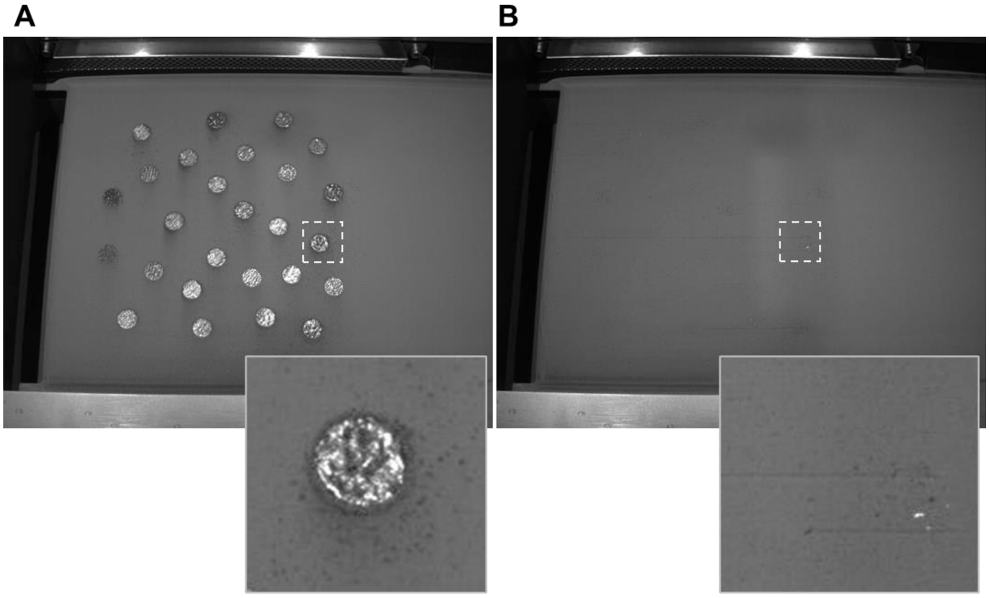

Figure 13: Sample outputs from powder bed monitoring after laser exposure (A) and after recoating (B). The inserts correspond to the highlighted patches in each image.

b. Melt pool monitoring

EOSTATE MeltPool monitoring (MPM) consists of two photodiodes mounted on-axis and off-axis. The photodiode mounted on-axis, i.e., coaxially with the laser beam, has a bandwidth that includes the visible and near-infrared spectra, while the photodiode mounted off-axis has a narrower bandwidth that only includes a fraction of the near-infrared spectrum. The signals are acquired in the time domain at 60 kHz but can be translated to spatial coordinates for enhanced data visualization (Figure 14).

The signal acquired through MPM was processed using two distinct algorithms. The signal's intensity characteristics were calculated as the moving average in windows including 600 data points, while the signal's dynamic characteristics were computed as the raw signal minus the moving average to highlight dynamic process changes.

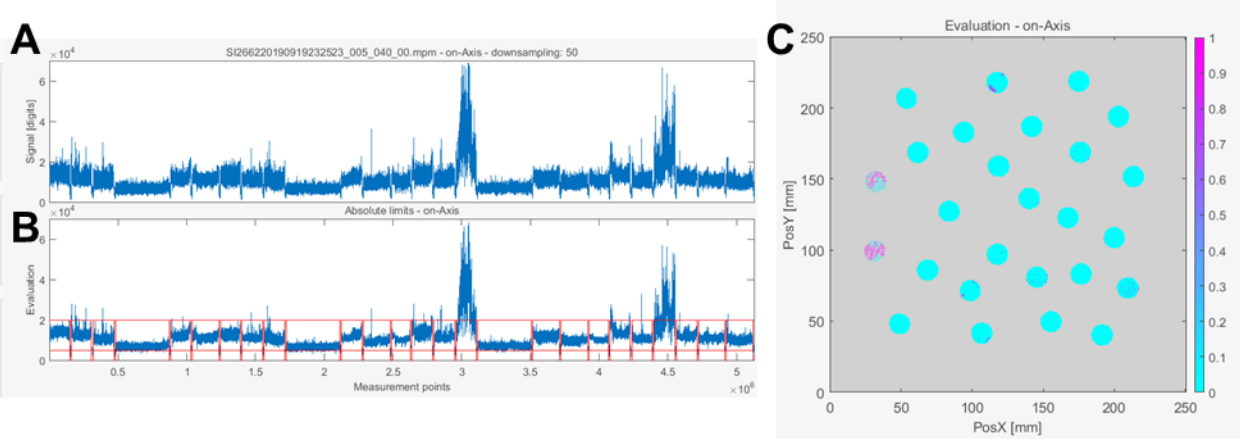

Figure 14: Sample output from MPM. The output consists of temporal signal intensity (A) but can be translated to spatial coordinates (C). The application of signal processing discriminates regions containing anomalies (B), also highlighted in the spatial representation.

c. Optical tomography

The EOSTATE Exposure optical tomography (OT) system is equipped with a 5-megapixel sCMOS (scientific complementary metal-oxide-semiconductor) camera positioned on top of the build chamber, covering the entire build area in its field of view. A bandpass filter of 900 nm ± 12.5 nm is placed on the camera to avoid detecting reflected laser, plasma radiation and visible light, considered environmental noise. During the laser exposure of a layer, images are acquired sequentially with the camera's shutter time set to 0.1 second. These images are combined in two distinct ways to output a single image per layer: each pixel in the output image either represents the maximum intensity (*MAX* output) or the integrated intensity (*INT* output) in a 125 µm × 125 µm patch of the build area during the exposure of the layer. Both outputs are exemplified in Figure 15 A and B for the same build layer.

Figure 15 C and D illustrates the different artifacts present in the OT outputs, with Figure 15C representing the regions highlighted in Figure 15 A and B. *MAX* images typically present a striped pattern that stems from hatching. In Figure 15 C, a stripe hatching pattern is used, and the dark line corresponds to the interface between adjacent stripes. In Figure 15 D, a chess hatching pattern is used, and the variation in hatching orientation is visible. In *INT* images, the hatching is typically not visible, and the interface between stripes, or patches in the case of chess-pattern hatching, are visible as bright lines. Identifying the typical artifacts present in each output is important for image analysis, as these features must be distinguished from those of interest.

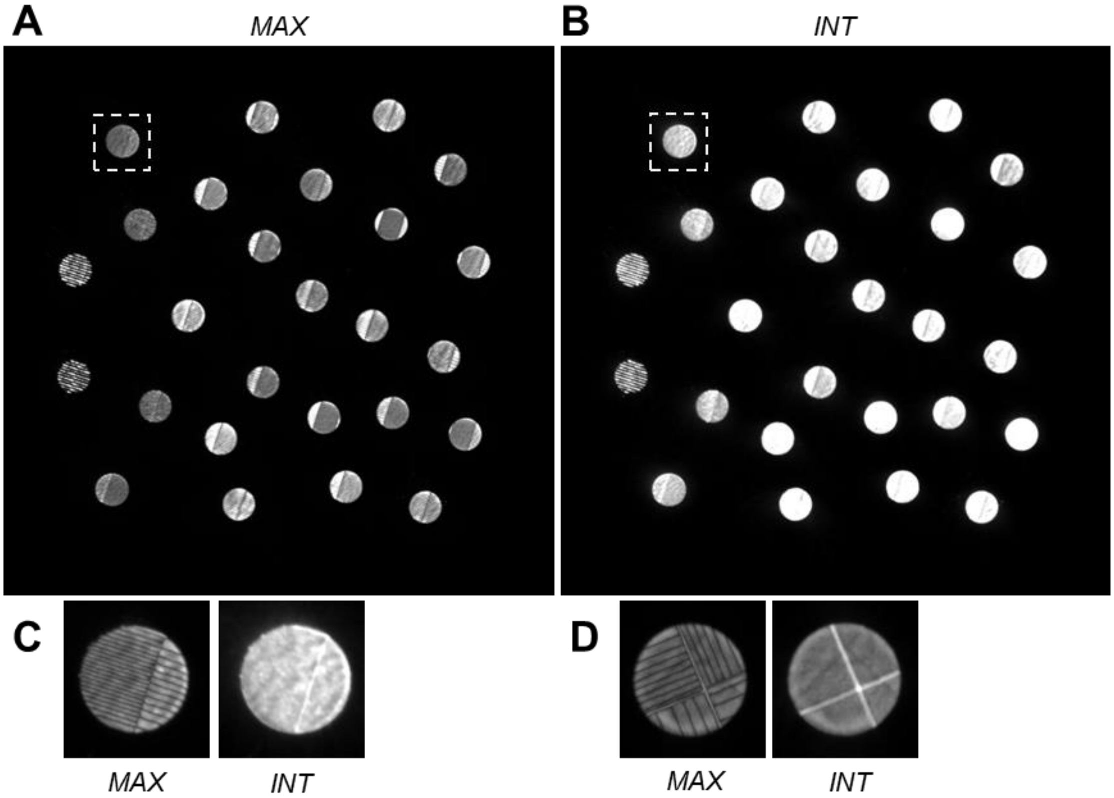

Figure 15: Sample *MAX* (A) and *INT* (B) outputs from optical tomography monitoring. The regions highlighted in (A) and (B) are shown in (C); in this case, a stripe hatching pattern was used. A chess hatching pattern was used in the specimens represented in (D).

In this thesis, image analysis methods have been chiefly employed in the output of EOSTATE Exposure OT. Data handling and image analysis were mostly performed in a Matlab environment. In the study of systematic defects, two data analysis approaches were taken. In the first one, the data analyzed was the intensity registered within part boundaries, not considering their spatial distribution. These intensities, also called grayvalues (GV), were treated as distributions, described by summary statistics and correlated to the defect population of each specimen (Paper II). Because it was not always possible to distinguish defective specimens from non-defective specimens with this approach, machine learning was incorporated into the analysis to cluster the summary statistics. With this, it was possible to distinguish specimens containing different predominant defect types. The approach described does not consider how the pixels are distributed in the image. To make use of this information, image analysis was used. One of the problems that can be handled through image analysis is classification, in which a classifier takes an input image and outputs a label. In this second approach to the study of systematic defects, a convolutional neural network was used to classify OT images into three categories of internal defects, whose presence was verified ex-situ through metallographic analysis (Paper III).

In the study of stochastic defects, image analysis was framed as a detection problem (Papers V-VIII, X, and XI). The redeposited spatters manifest as bright blobs on a darker background and can be detected on an image $I(x, y)$ using a Laplacian of Gaussian (LoG) operator [103], expressed in equation (1). The standard deviation σ is selected so the filtered image converges to local extrema upon detection of a spatter redeposit. After filtering, non-minimum suppression was applied to ensure unique detections in each spatter. The process is schematized in Figure 16.

$$LoG(x, y) = -\frac{1}{\pi\sigma^4}\left[1 - \frac{x^2 + y^2}{2\sigma^2}\right] \exp\left(-\frac{x^2 + y^2}{2\sigma^2}\right) \tag{1}$$

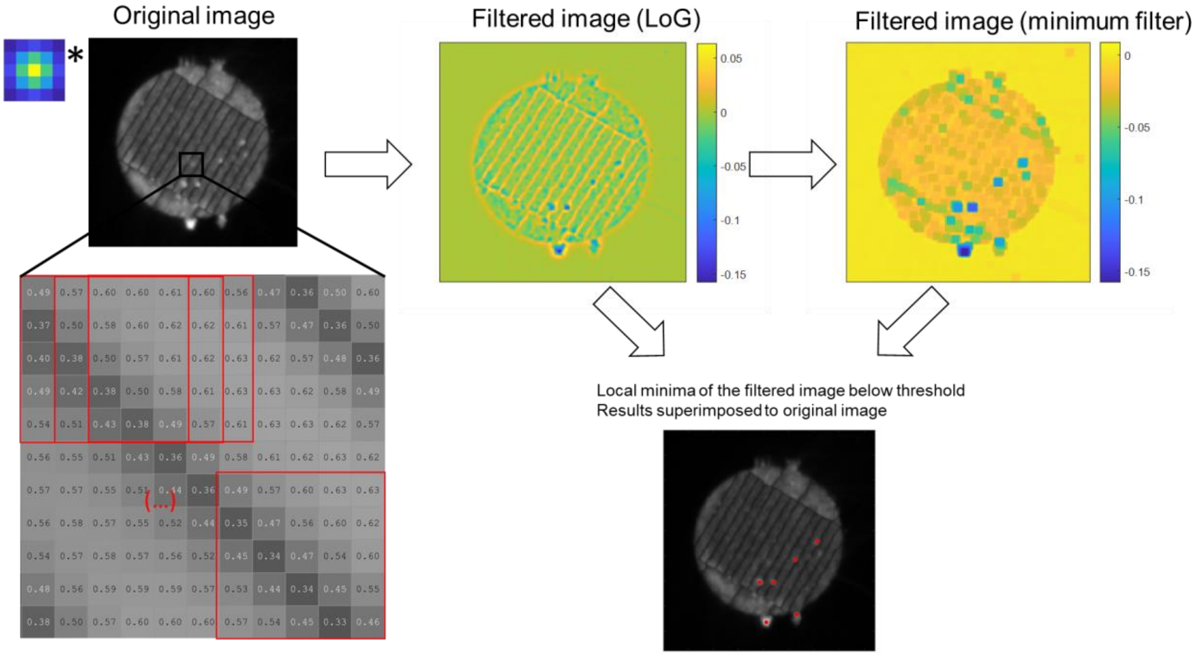
Original image
*
Filtered image (LoG)
0.05
0
-0.05
-0.1
-0.15
Filtered image (minimum filter)
0
-0.05
-0.1
-0.15
Local minima of the filtered image below threshold
Results superimposed to original image
(...)

0.49	0.57	0.60	0.60	0.61	0.60	0.56	0.47	0.36	0.50	0.60
0.37	0.50	0.58	0.60	0.62	0.62	0.61	0.57	0.47	0.36	0.50
0.40	0.38	0.50	0.57	0.61	0.62	0.63	0.62	0.57	0.48	0.36
0.49	0.42	0.38	0.50	0.58	0.61	0.63	0.63	0.62	0.58	0.49
0.54	0.51	0.43	0.38	0.49	0.57	0.61	0.63	0.63	0.62	0.57
0.56	0.55	0.51	0.43	0.36	0.49	0.58	0.61	0.62	0.63	0.62
0.57	0.57	0.55	0.51	0.44	0.36	0.49	0.57	0.60	0.63	0.63
0.56	0.58	0.57	0.55	0.52	0.44	0.35	0.47	0.56	0.60	0.62
0.54	0.57	0.58	0.57	0.56	0.52	0.45	0.34	0.47	0.54	0.60
0.48	0.56	0.59	0.59	0.59	0.57	0.53	0.44	0.34	0.45	0.55
0.38	0.50	0.57	0.60	0.60	0.60	0.57	0.54	0.45	0.33	0.46

Figure 16: Schematic workflow of the detection of spatter redeposits on OT images.

6.4 Ex-situ analytical techniques

a. Metallographic specimen preparation

Specimen preparation was conducted by standard metallographic procedures: plane grinding with 320-grit sandpaper, subsequent fine grinding with 9 µm diamond suspension on a Struers MD-Largo surface, and final colloidal silica polishing. Electrolytic etching was performed in a solution with 5 g oxalic acid mixed with 95 ml reagent grade HCl.

b. Microscopy

In this thesis, microscopy was mainly used to observe and measure internal defects but also to measure melt pool dimensions, image powder and spatter samples and fracture surfaces. Three different techniques were used: light optical microscopy (LOM), stereo optical microscopy (SOM), and scanning electron microscopy (SEM).

Light optical microscopy

The specimens in which quantification and measurement of internal defects were performed had a relatively large cross-section of approximately 10 mm × 20 mm. Each cross-section was fully imaged in the unetched condition using the stitching tool in Zeiss Axioscope 7 light optical microscope (LOM) at 50x magnification, yielding detectable features down to 0.88 µm, pixel size. First, the resulting LOM images were binarized, thus discriminating solid material from defects. Then, the properties of the features corresponding to defects were measured individually and automatically, with a single defect corresponding to a contiguous region in the binarized image. Among the quantities measured is the defect length, also referred to as defect size, as well as the area fraction of defects, which corresponds to the volume fraction of defects, assuming that the area is representative of the bulk.

Scanning electron microscopy

In scanning electron microscopy (SEM), a focused electron beam is used to scan the surface and near-surface of the specimens under analysis. The interaction between the electron beam and the material under observation generates different signals, among which secondary electrons and backscattered electrons, used for imaging, and X-rays, used for chemical analysis.

The SEM work done in this thesis employed a field emission gun scanning electron microscope (FEG-SEM) Leo Gemini 1550. SEM was used for microstructural characterization of the as-printed Hastelloy X, analysis of fracture surfaces, and characterization of powder and spatters in terms of morphology and surface morphology. Electron backscatter diffraction (EBSD) is a technique integrated into SEM systems that provides data on the crystallography of materials, for example, grain size, shape and orientation, and allows the identification of phases and texture.

c. Non-destructive evaluation

Ultrasonic inspection

Ultrasonic inspection is a mature technology widely used in industry to detect defects. In this thesis, its output was compared to the overall distribution of internal defects detected through the monitoring system. The ultrasonic inspection was performed as a linear scan transversally to the build direction, with a 64-element linear phased array longitudinal wave probe (Zetec LM-5MHz) fixed at a single position on each specimen analyzed. The ultrasonic waves were emitted from an aperture of 16 probe elements and propagated into the specimen with a 0-degree refraction angle. Proper delay laws were applied to realize the beam focusing at one scan position. In order to cover the entire region of each build, the aperture travels along the whole array with a step of 1 element. The ultrasonic inspection data were collected and recorded under a sampling frequency of 100 MHz by a corresponding data acquisition hardware unit labeled TOPAZ64 from Zetec and then post-possessed using UltraVision software. The longitudinal wave speed in Hastelloy X is about 5700 m/s. Using the phased array probe with center frequency of 5 MHz, the wavelength in this material is about 1.1 mm, which allowed for the detection of defects larger than 500 µm.

X-ray computed tomography

X-ray computed tomography (XCT) was used to measure the internal defect populations of selected, relatively thin specimens, as Hastelloy X has a high X-ray absorption coefficient. The equipment used was a custom-developed X-ray CT system consisting of a microfocus X-ray tube (XWT-190-TCNF, X-RAY WorX), a 4000 × 4000 px^2 digital X-ray detector (XRD 1611 CP3, Perkin Elmer), and air-bearing motion axes [104] [105]. XCT data analysis was performed in VG Studio MAX 3.4 (Volume Graphics). The volume data were filtered with a 3 × 3 × 3 median filter, and the outer sample surface was segmented using a gradient-based surface determination algorithm. Porosity analysis was performed using the VGEasyPore module.

d. Surface characterization

Due to the high surface-to-volume ratio combined with interaction with a laser beam in an atmosphere containing oxygen, surface characteristics of powder are important in LPBF. Surface characterization was performed via X-ray photoelectron spectroscopy (XPS) and Auger electron spectroscopy (AES).

X-ray photoelectron spectroscopy

X-ray photoelectron spectroscopy (XPS) is a surface analysis technique used in this thesis to identify the chemical state and estimate the concentrations of the elements present on the surface of powder and spatter particles. The equipment used was a PHI 5500 VersaProbe III scanning XPS microprobe (ULVAC-PHI) equipped with monochromatic aluminum Kα X-ray source (1486.6 eV).

Auger electron spectroscopy

AES is a surface analysis technique with higher lateral analytical resolution used in this thesis to investigate specific regions of powder and spatter particles. The AES analyses were conducted with a PHI 700 scanning Auger nanoprobe (ULVAC-PHI). The electron accelerating voltage was 10 kV, and the beam current was 10 nA, enabling a nominal analytical lateral resolution of ~20 nm.

e. Bulk chemical analysis

Bulk chemical analysis was used in this thesis to measure bulk oxygen and nitrogen contents in consolidated LPBF parts. The analyses were performed using a LECO ON836 at Höganäs AB. Small samples were extracted from the parts, placed into a graphite crucible, and heated to release analyte gases, which were then detected by non-dispersive infrared (NDIR) cells.

f. Mechanical tests

Mechanical tests were performed to assess the mechanical performance of LPBF of virtually defect-free Hastelloy X with varying microstructures (Paper IV) and of Hastelloy X affected by spatter redeposition (Papers VIII, X, and XI).

Tensile tests

All tensile tests reported in this thesis were performed at room temperature using as-printed specimens manufactured with the main axis oriented along the build direction. The tests pertaining to Paper IV were performed on an Instron 8501 servo-hydraulic machine and with an Instron 2630–102 axial clip-on static mounted on the gauge length for measuring the uniaxial strain. The tests were performed at a strain rate of $2 \cdot 10^{-4}$ s^{-1} in accordance with the ASTM E8/E8M guidelines.

The tests pertaining to Papers VIII and X were done according to the ISO 6892-1 standard on an Instron 5582 universal electromechanical testing machine according to machine with a 100 kN load cell at a constant strain rate of $2 \cdot 10^{-3}$ s^{-1}.

Fatigue tests

The fatigue tests reported in this thesis were performed at room temperature and according to ISO 1099, using specimens printed with the main axis oriented along the build direction in the machined and polished condition. Fully-reversed ($R = -1$) stress-controlled fatigue tests with a frequency of 10 Hz were conducted at two stress ranges, 800 MPa and 900 MPa. These tests were performed on an Instron 5582 universal electromechanical testing machine.

CHAPTER 7
SUMMARY OF RESULTS

This chapter summarizes the results of the appended papers. **Papers I - IV** address systematic defects. In **Paper I**, the defect populations and melt pool geometries were mapped in the process parameter space. The capabilities of the melt pool monitoring system of predicting melt pool geometry, melt pool dynamics, and internal defects were then evaluated. The data collected ex-situ in **Paper I** were used to investigate the correlation between OT grayvalues and defect type and content in **Paper II**, and classify the images acquired through the OT monitoring system into the predominant defect type encountered in the specimens in **Paper III**. In **Paper IV**, the virtually defect-free region of the process parameter space identified in **Paper I** was studied in detail to assess the variation of microstructure and properties from a productivity-focused perspective.

Papers V - XI address stochastic defects. **Paper V** investigated the formation and detection of stochastic defects caused by the redeposition of spatters on the powder bed in builds where productivity was increased. A method for detecting spatters and an initial correlation between defects and detections were established, addressing patterns across the build area and process. In **Paper VI**, a detailed investigation was conducted, and the exact correspondence between individual detections in OT images and lack of fusion defects was established. Given the variation in defect content among builds observed in **Paper V**, spatter particles collected in these builds were investigated in **Paper VII**, as well as the OT signal external to part boundaries, to obtain insights on the formation and trajectories of these particles. The effect of spatter redeposition and associated defect formation on the mechanical properties of Hastelloy X were addressed in **Paper VIII**, where tensile and fatigue tests were conducted. A potential mitigation strategy for spatter-induced defects was investigated in **Papers IX** and **X**, where the oxygen content in the process atmosphere was restricted to a maximum of 50 ppm. In **Paper IX**, spatter particles were thoroughly characterized to better understand the effect of oxygen content present in the process atmosphere on their surface characteristics. In **Paper X**, the effect of the reduction of oxygen content was verified in terms of defect formation and mechanical properties. In **Paper XI**, another defect mitigation strategy was proposed and investigated: modifying the laser scan pattern to aid spatter removal from the build area.

7.1 Systematic defects

a. Mapping

In **Paper I**, a comprehensive design of experiments was employed on the manufacturing of Hastelloy X specimens, exploring a wide range of the process parameter space. In-situ monitoring of the melt pools was conducted throughout the manufacturing process. Subsequent ex-situ evaluations involved measurements of melt pool widths and depths, and analysis of internal defects. The volume fraction of defects at each experimental point can be seen in Table 4, in which the transition between keyhole and conduction is represented with a dashed line.

The investigation delved into the analysis of melt pool geometry, signal characteristics, and internal defects. These analyses were conducted by systematically varying one parameter at a time, independently for both keyhole and conduction regimes (Figure 17). In the examples illustrated, the laser power is the only process parameter altered. Through this factor-by-factor analysis, it was discerned that the signals acquired via melt pool monitoring exhibited intensities that correlated with the average dimensions of the melt pool. Moreover, these signals demonstrated more pronounced dynamic attributes in response to process conditions that promoted spatter generation, coinciding with an escalation in energy input.

A consistent trend of heightened scatter in melt pool dimensions emerged in specimens featuring a greater volume fraction of defects. This increased variability in melt pool dimensions was ascribed to the progressively uneven substrate onto which the melt pools were deposited, owing to the presence of larger and more prevalent internal defects. However, it is noteworthy that the scatter in melt pool dimensions and deliberately introduced systematic internal defects remained undistinguishable through melt pool monitoring.

Table 4 Volume fraction of defects (%) across the process parameter space. Laser power, scan speed and layer thickness are varied systematically. The dashed lines indicate the location of the transition between keyhole and conduction fusion. "N/A" indicates manufacturing could not be completed due to extreme processing conditions. The highlighted cells correspond to process conditions considered desirable. From **Papers I**[106] **/ III**[44].

			Laser scan speed (mm/s)							
			200	**400**	**600**	**800**	**1000**	**1200**	**1400**	**1600**
Laser power: 100 W	**Nominal layer thickness (µm)**	**20**	0.39	0.01	0.31	1.41	5.48	7.97	11.6	14.2
		40	0.14	0.76	0.78	5.95	14.3	19.4	27.3	32.1
		80	5.61	11.7	16.5	26.8	35.1	45.4	N/A	N/A
Laser power: 200 W	**Nominal layer thickness (µm)**	**20**	4.47	2.55	0.03	0.01	<0.01	0.19	0.63	1.27
		40	5.12	2.77	0.02	0.01	0.09	0.44	1.67	4.51
		80	6.79	2.19	0.11	0.31	6.90	12.1	18.8	25.6
Laser power: 300 W	**Nominal layer thickness (µm)**	**20**	N/A	2.34	0.44	<0.01	<0.01	0.02	0.10	0.14
		40	3.31	3.50	0.30	<0.01	0.01	0.04	0.12	0.26
		80	4.50	3.19	0.35	0.01	0.03	0.06	0.39	2.53

b. Prediction based on grayvalues

In **Paper II**, the OT output was analyzed in terms of pixel intensity values, also denominated *grayvalues* (GV). The OT *MAX* image from each specimen at each manufacturing layer was masked to exclude signal external to nominal part boundaries, and a set of summary statistics were computed for each of the corresponding distributions, as per the scheme in Figure 18. Summary statistics condensate the information contained in a distribution of 5.025 points (the number of pixels in an OT image representing a single specimen in a single layer) and represent this distribution with a few values – in this case:

- The median, representing the central tendency,
- The 1st and 99th percentiles, representing the distributions' extremes (minimum and maximum, respectively).

These summary statistics vary in each manufacturing layer for a single specimen, even if the processing conditions are constant. The magnitude of this variation across processing conditions and the distributions of the summary statistics considering the entire manufacturing process were assessed and correlated to the defect populations. It was found that, generally, higher GV are registered in specimens containing keyhole pores, lower GV in specimens with lack of fusion, and intermediate GV in defect-free specimens. However, the summary statistics of GV distributions can extensively overlap with those from defect-free specimens, as observed in Figure 19. The extensive overlap challenges the formulation of simple rules to distinguish defective and non-defective specimens. Because of that, complementarily to **Paper II**[107], the extracted summary statistics were clustered via k-means clustering (Figure 20) and the assigned clusters were compared to the categories determined via metallographic analysis. With that, it was determined that 92% of the data points were correctly clustered.

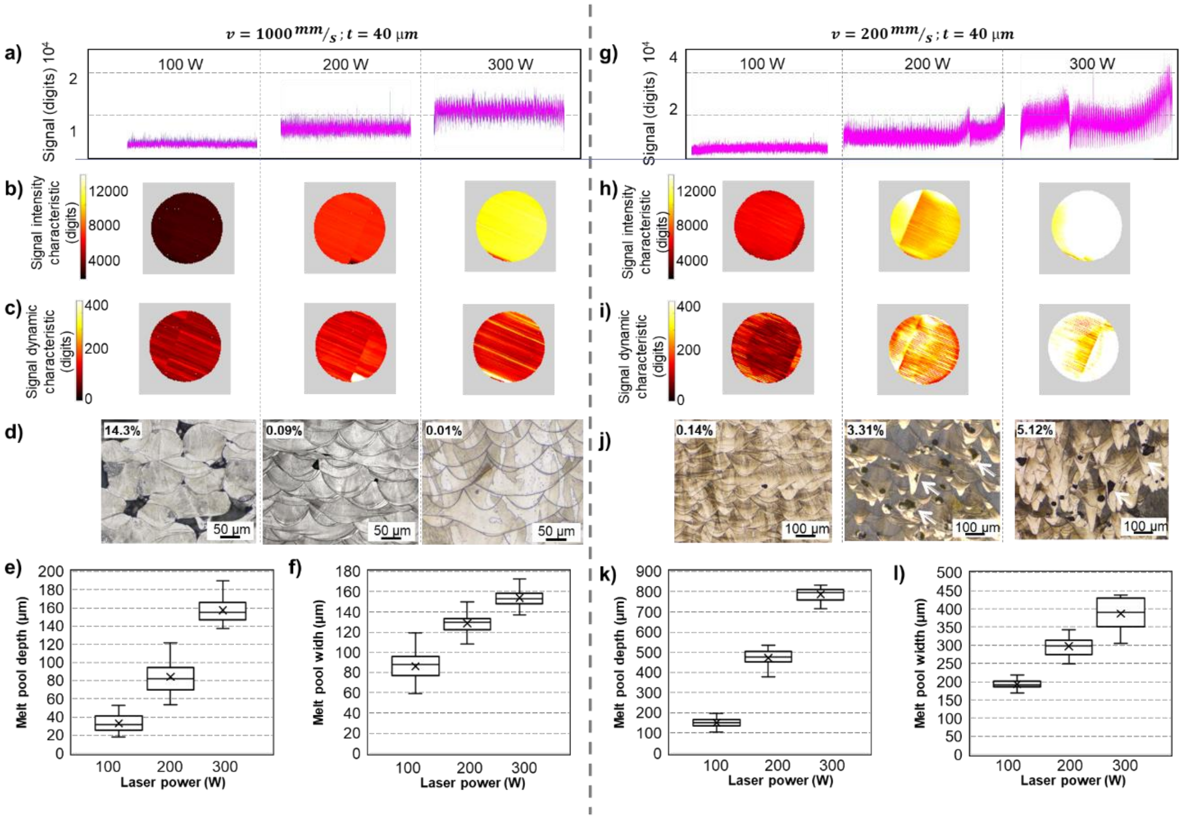

Figure 17: Influence of laser power on melt pool signal characteristics, melt pool dimensions and defect populations in the conduction (a-f) and keyhole regimes (g-l). The specimens were manufactured with varying laser power (100 W, 200 W and 300 W). The plots in a) and g) show the MPM output in temporal x-coordinate. The signal translated to spatial coordinates is shown in b) and h). The signals processed to highlight regions of high melt pool dynamics are shown in c) and i). The microstructures of the corresponding specimens are shown in d) and j), where the volume fraction of defects is indicated. The influence of laser power variation on melt pool depths and widths are shown in e), f), k) and l). Adapted from **Paper I** [106].

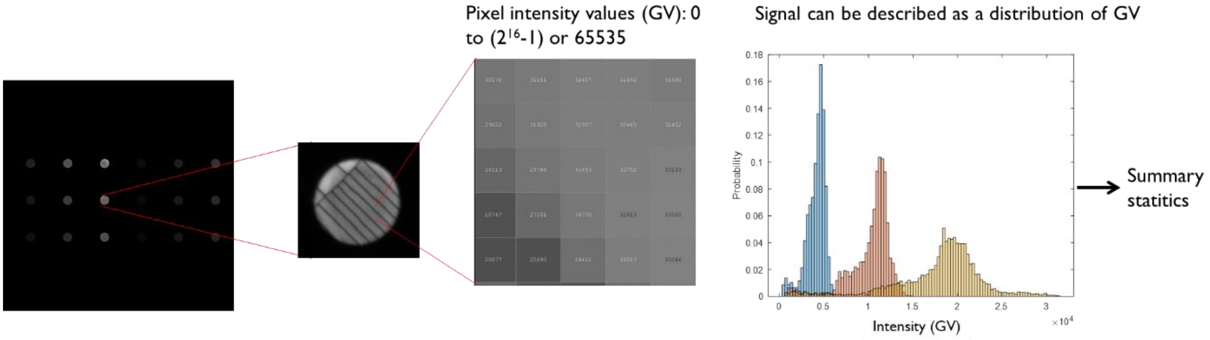
Pixel intensity values (GV): 0 to (2¹⁶-1) or 65535
Signal can be described as a distribution of GV
Probability
Intensity (GV)
×10⁴
Summary statitics

Figure 18: Schematic data extraction workflow from OT images, focusing on GV.

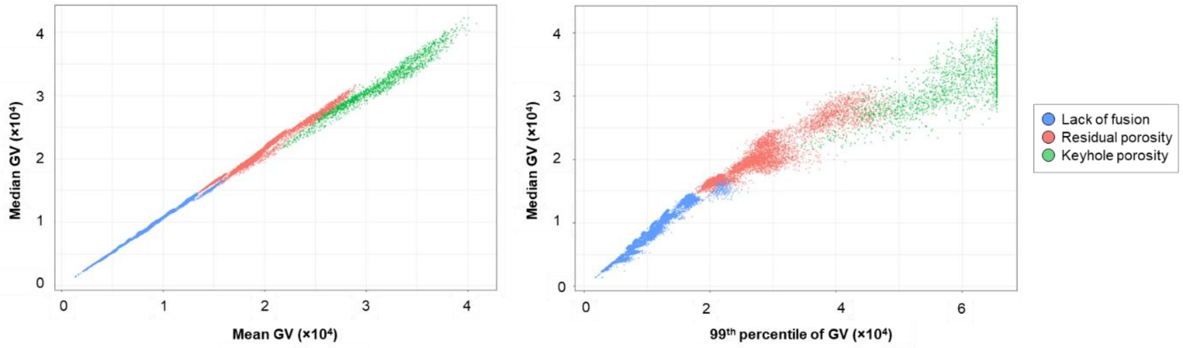

Figure 19: Summary statistics of GV of whole specimens manufactured with varying processing parameters. From **Paper II** [107].

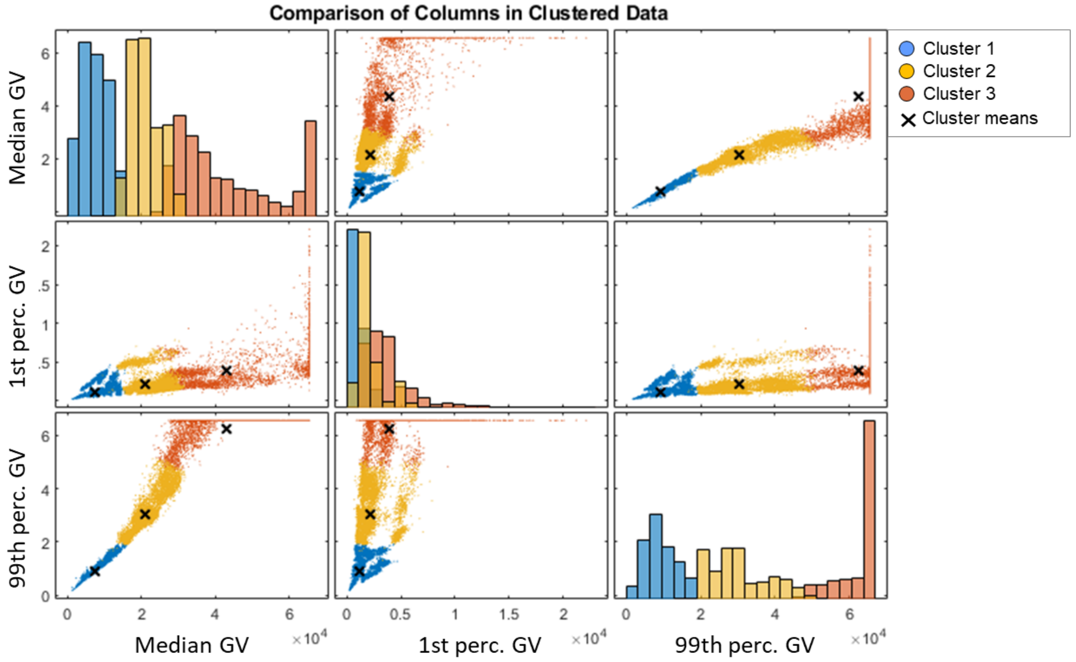

Figure 20: Clustering summary statistics of GV distributions. Cluster 1 corresponds to specimens containing lack of fusion; cluster 2 to virtually defect-free specimens; cluster 3 to specimens containing keyhole pores.

c. Classification using machine learning

Since the need and benefit of using machine learning to the problem of defect detection were identified, another machine learning approach was taken to analyze the data, considering the spatial component of OT images. In **Paper III**, a fully convolutional neural network (CNN) was designed to classify OT images per the main defect type identified through metallographic analysis.

The OT images were divided into patches of constant size centered in each specimen and only containing signals emitted from that specimen (Figure 21a, c). All patches corresponding to the same specimen received the same label (Figure 21c) since the defects are generated systematically due to process parameters (Figure 21b), and each layer is assumed to be representative of the resulting defect distribution. The labeled examples are partitioned into three sets: the training set, used to fit the parameters in the network; the validation set, which provides an evaluation of the model during the training process and prevents overfitting (Figure 21d); and the test set, set apart in previous stages for the evaluation of the final model.

The validation accuracy of the network is 97.99%. In order to estimate the performance of the network in practice, it was applied to the test set, which consists of 1,122 images previously set apart for this purpose. The confusion matrix presented in Figure 21e describes the performance, which shows the overall accuracy in the test set (97.8%), as well as precision, false discovery rate, recall, and false-negative rate for each category. Thus, it is demonstrated that it is possible to distinguish virtually defect-free material from material containing systematic defects based on monitoring data acquired in situ with high accuracy.

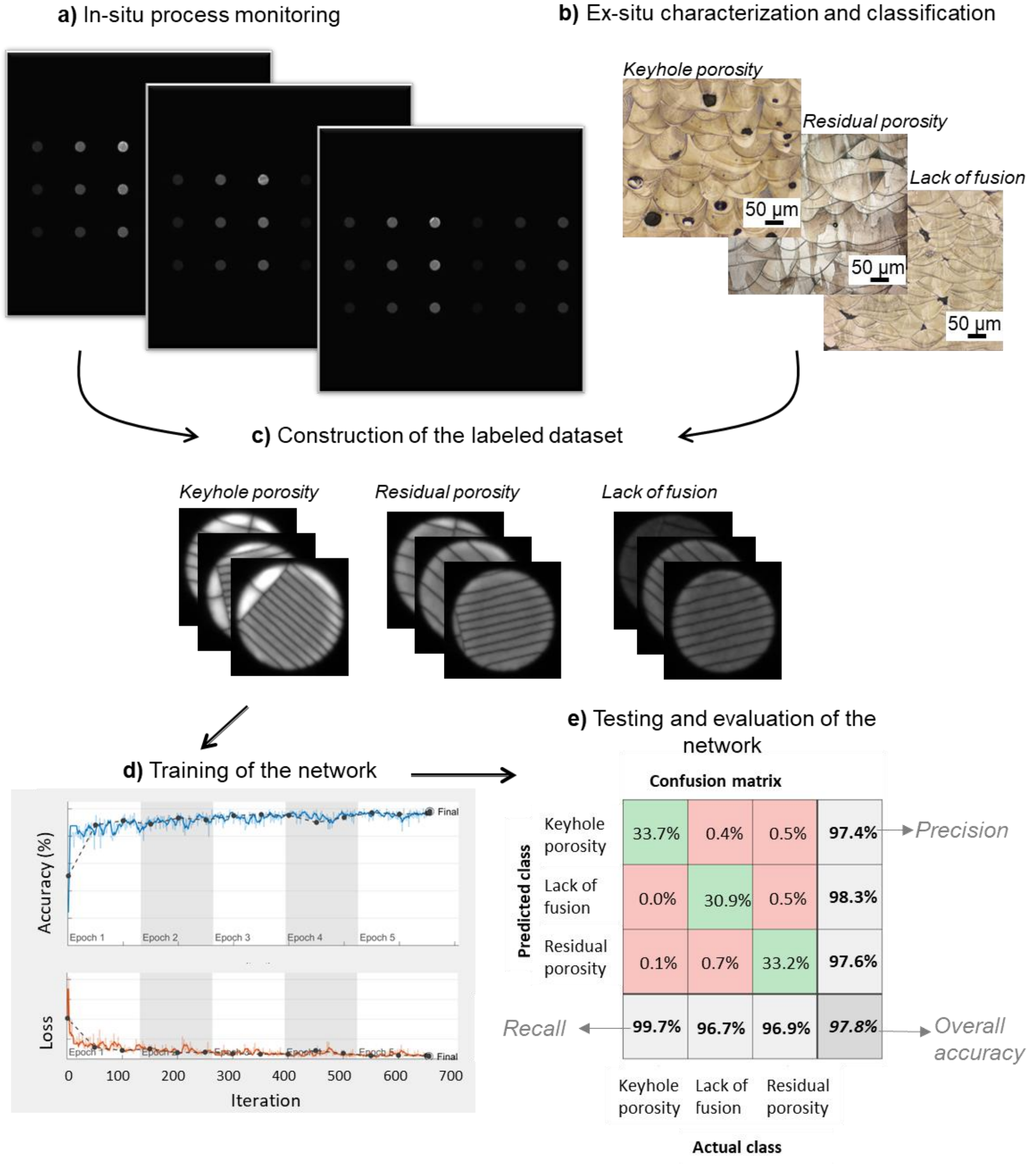
a) In-situ process monitoring
b) Ex-situ characterization and classification
Keyhole porosity
Residual porosity
Lack of fusion
50 µm
50 µm
50 µm
c) Construction of the labeled dataset
Keyhole porosity
Residual porosity
Lack of fusion
d) Training of the network
Accuracy (%)
Loss
Epoch 1
Epoch 2
Epoch 3
Epoch 4
Epoch 5
Final
0
100
200
300
400
500
600
700
Iteration
e) Testing and evaluation of the network
Confusion matrix
Predicted class
Keyhole porosity
Lack of fusion
Residual porosity
33.7%
0.4%
0.5%
97.4%
Precision
0.0%
30.9%
0.5%
98.3%
0.1%
0.7%
33.2%
97.6%
Recall
99.7%
96.7%
96.9%
97.8%
Overall accuracy
Keyhole porosity
Lack of fusion
Residual porosity
Actual class

Figure 21: Schematic workflow of **Paper III** [44].

7.2 Productivity enhancement in the defect-free zone

With the work performed in **Papers I-III**, the quantity, type and size of process parameter-driven defects were characterized for Hastelloy X, and their detectability was ensured. Moreover, multiple processing conditions that result in virtually defect-free material were identified (highlighted in Table 4). These are considered the "desirable" process conditions, as defect avoidance is achieved through their employment. However, within the range of desirable processing conditions, variability in microstructure, properties and achievable build rates are expected. These factors are investigated in **Paper IV** from a productivity perspective.

Considering the absence of a unified approach for the increase of the build rates based on process parameters, the first goal of **Paper IV** was to obtain a simplified parametrization of the build rate. For that, it was assumed that the build time is mainly governed by exposure of the bulk region and that the infill parameters and transition time between layers are invariable throughout a build. With these factors considered, the build rate can be expressed as:

$$B = \frac{Rvht}{R + \Delta\tau_{tr} vh} \tag{2}$$

Where v is the laser scan speed, h is the hatch spacing, t is the layer thickness, $\Delta\tau_{tr}$ is the time interval for the transition between layers, and R is the average utilization of the build area, which can also be expressed as the ratio between the volume of the build envelope and build height.

Plugging the processing conditions highlighted in Table 4 into Equation (2), the build rates attainable when still producing virtually defect-free material were obtained. The results can be visualized in Figure 22a. The influence of productivity increase in the microstructure of Hastelloy X was determined. As multiple process parameters were varied to increase productivity, some microstructural features vary within the defined process window (Figure 22b-f). For example, the material produced with the highest productivity presents the most random grain orientation and pockets of fine grains at the bottom of the melt pools (Figure 22b). For the lowest productivity, grain growth and a stronger ⟨101⟩ orientation of the larger grains were observed (Figure 22a).

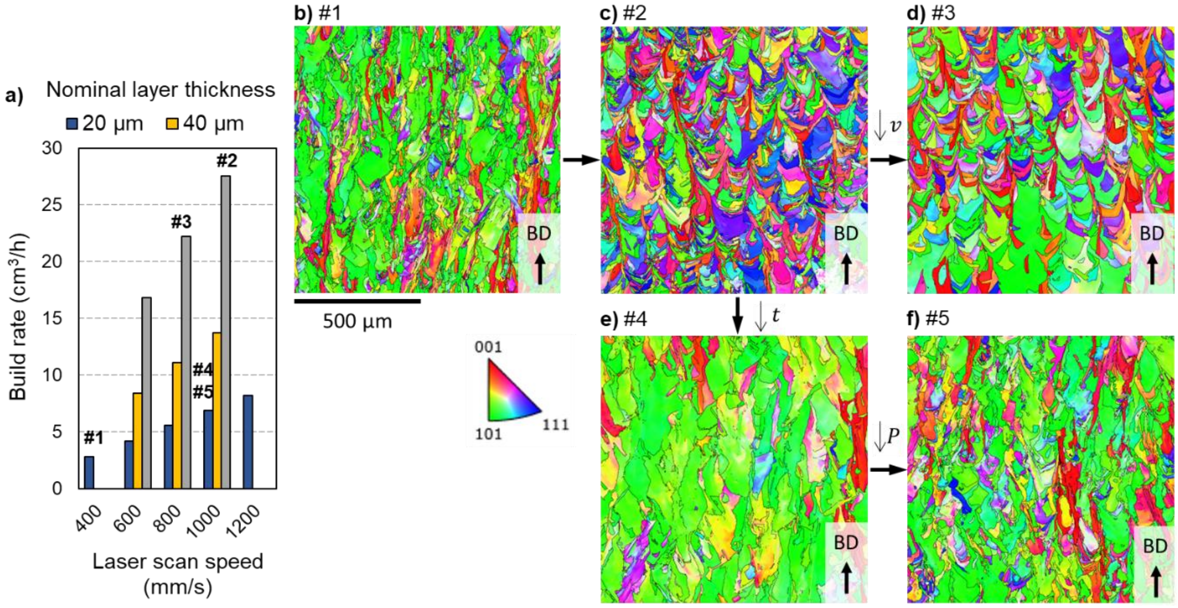

Figure 22: (a) Build rates (cm^3/h) for the sets of process parameters in the process window. EBSD orientation maps in IPF coloring for material manufactured with (b) highest productivity (P=300 W, v=1000 mm/s, t=0.08 mm and lowest productivity in the study (P=100 W, v=400 mm/s, t=0.02 mm). Adapted from **Paper IV**[73].

7.3 Stochastic defects

a. Macroscale

Upon landing on regions of the powder bed exposed by the laser beam, spatters can potentially generate internal defects. Given the inherently stochastic nature of defects induced by spatter, the real-time detection of spatter redeposition becomes crucial. In the context of **Paper V**, three separate LPBF builds were executed using Hastelloy X, wherein parameters were fine-tuned to achieve materials with nominal full density at three distinct layer thicknesses: 80 µm, 120 µm, and 150 µm. Throughout the build process, EOS OT Exposure was employed for continuous monitoring. The analysis of monitoring images enabled identifying and quantifying redeposited spatters, thereby facilitating the determination of their spatial distribution.

It was determined that the chosen nominal layer thickness significantly influenced the occurrence and spatial arrangement of redeposited spatters. Specifically, a preference for redeposition near the gas outlet was observed. Notably, as the layer thickness increased, a greater quantity of redeposited spatters was discerned, encompassing a larger area within the build region. This observation is depicted in Figure 23. Importantly, this finding presents a notable constraint on the potential enhancement of LPBF productivity.

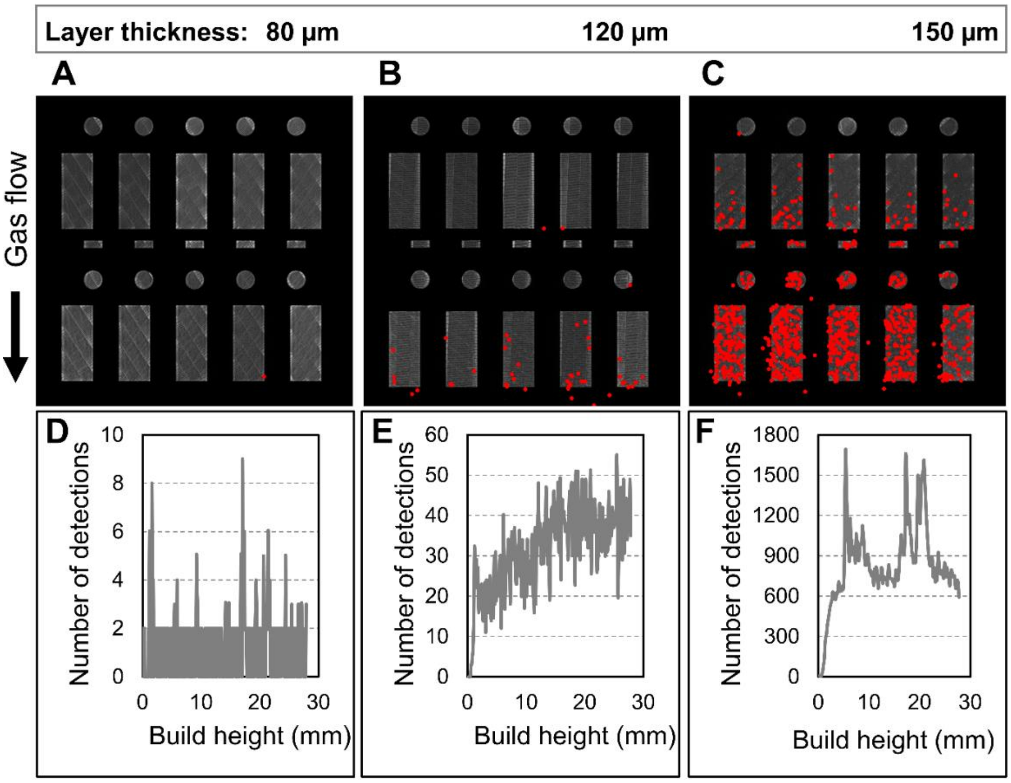

Figure 23: Redeposited spatters in builds with varying layer thicknesses. Detections (in red) on builds with layer thicknesses 80 µm (A), 120 µm (B) and 150 µm (C). The number of detections per layer versus build height is presented in D – F. From **Paper V**[26].

It was observed that the locations of spatter redeposition depend on the laser scan direction, as illustrated in Figure 24. OT image patches representing laser exposure in distinct directions are seen in Figure 24a, c. These images are modified in Figure 24b and d, respectively, to show the trajectory of spatter particles. The initial trajectory is parallel to the scan lines and then aligns with the direction of the gas flow. Spatters were found to redeposit preferentially on the side of the build plate where their initial trajectories were also partially aligned against the gas flow (Figure 24e).

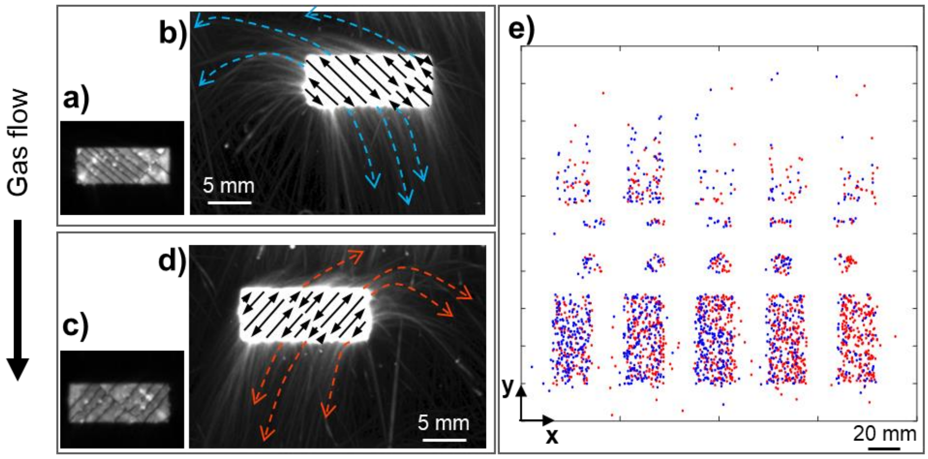

Figure 24: Distribution of redeposited spatter on the build area depending on the orientation of the laser scan vectors. The stripe orientations seen in (a) and (c) determine the initial trajectory of spatters that then align with the gas flow ((b) and (d)). The spatter redeposits on the layer with stripe orientation as (a) are represented in blue, while the detections stemming from stripe orientation as (c) are represented in red (e). From **Paper V**[26].

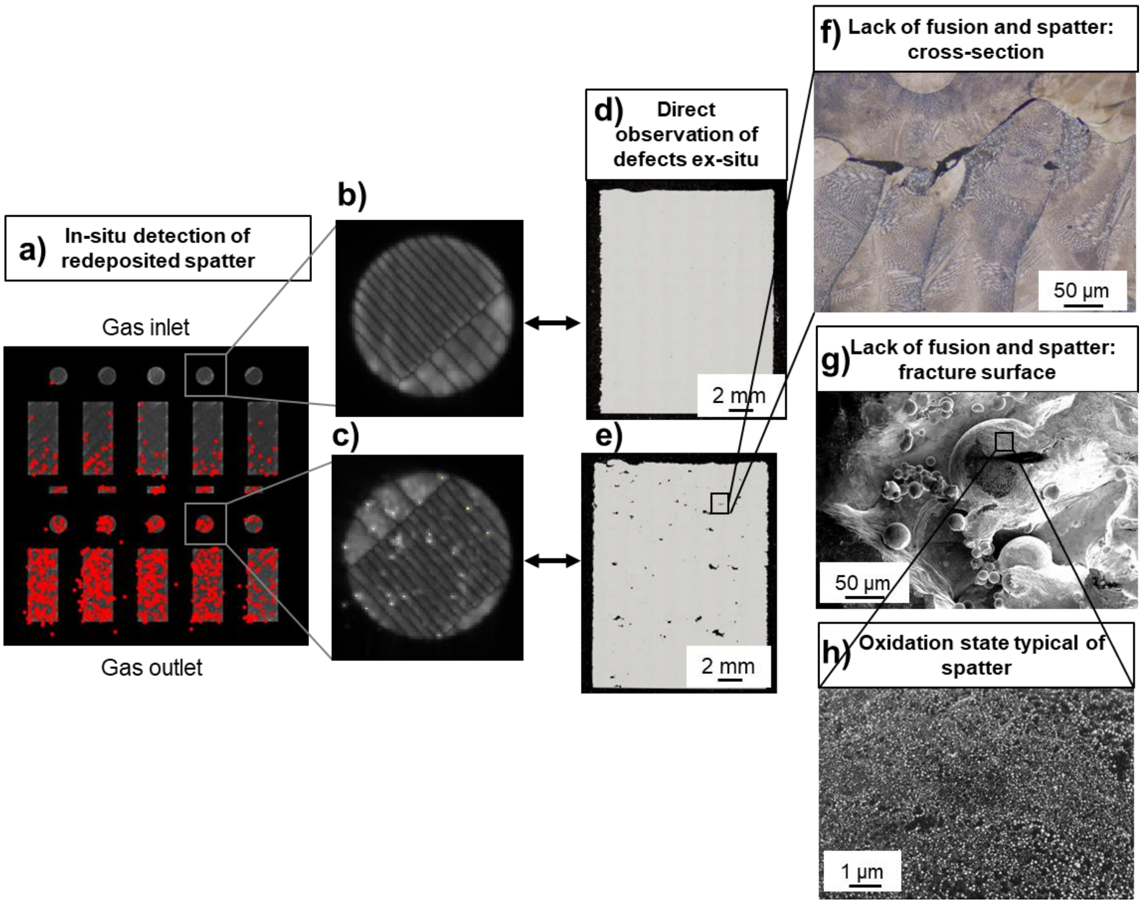
a) In-situ detection of redeposited spatter
Gas inlet
Gas outlet
b)
c)
d) Direct observation of defects ex-situ
2 mm
e)
2 mm
f) Lack of fusion and spatter: cross-section
50 µm
g) Lack of fusion and spatter: fracture surface
50 µm
h) Oxidation state typical of spatter
1 µm

Figure 25: Correspondence between detections of spatter redeposits and internal defects. Considering the build layout (a), few spatter redeposits are detected in specimens manufactured near the gas inlet (b). Metallographic analysis of these specimens reveals no major internal defects (d). Detections of spatter redeposits can be abundant in specimens manufactured near the gas outlet (c), and these specimens present large internal defects (e). Particles are observed adjacent to lack of fusion defects on cross-sections (f) and fracture surfaces (g). Some of these particles have surface oxides (h). Adapted from **Paper V**[26].

A combination of destructive and non-destructive testing methods was employed to establish the link between identified redeposited spatter and internal defects. The results of both analyses consistently demonstrated that specimens exhibiting minimal occurrences of spatter redeposition exhibited no significant internal defects. Conversely, regions exhibiting prominent detections through in-situ monitoring were associated with instances of lack of fusion, as depicted in Figure 25. Upon observation of the cross-sections of the specimens, distinct features came to light. Rounded particles displaying a dendritic structure, often possessing diameters notably exceeding those of the original feedstock powder, were observed near areas of incomplete fusion (Figure 25f). This observation serves as evidence of spatter involvement in generating these defects. Further substantiating this finding, the fracture surface was examined (Figure 25g-h). The particles situated near lack of fusion defects exhibited the same oxidation state as spatter that had been independently analyzed, thus providing conclusive confirmation of spatters' influence in forming defects.

Due to the striking differences in defect formation among builds where different nominal layer thicknesses were used, the spatter particles collected in each of these builds were further analyzed in **Paper VII** to determine whether any characteristics of the particles vary among builds. The OT images were also re-analyzed, focusing on the signal external to part boundaries to qualitatively evaluate the spatter ejections across builds (Figure 26). As the nominal layer thickness increases, more spatter particles are generated per layer, and thicker oxides, richer in Al and Ti, cover the particles, on average.

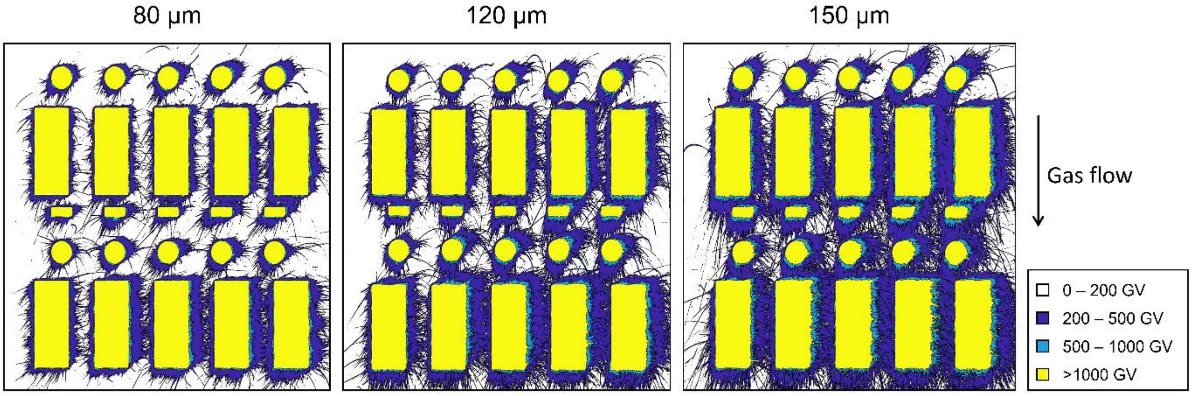

Figure 26: Contour plots of the signal intensity registered via OT of a single representative layer of builds performed with nominal layer thicknesses 80 μm, 120 μm, and 150 μm. From **Paper VII** [108].

b. Microscale

Paper VI establishes a more exact correspondence between detections and defects. For that, smaller volumes of material were analyzed via OT in-situ monitoring and ex-situ XCT. The lack of fusion defects measured via XCT matched the detections in OT images in specimens manufactured under several processing conditions. A visual comparison between lack of fusion defects identified in XCT and detections in OT images is provided in Figure 27, which represents randomly selected instances from multiple specimens. There is an evident correspondence between spatter detections and defects revealed by XCT, especially larger defects. A fair spatial correspondence between both detections is present, but the match is not exact, as the features detected are distinct (defects for XCT and spatters for OT). As spatter particles induce defects, a slight offset is expected and observed.

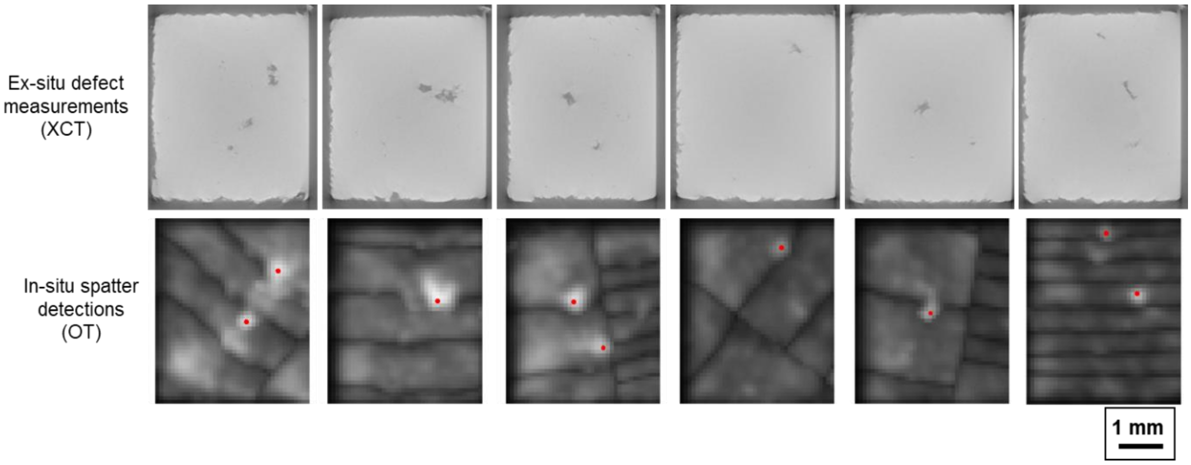
Ex-situ defect measurements (XCT)
In-situ spatter detections (OT)
1 mm

Figure 27: Visual correspondence between XCT slices (top) and OT images overlaid with detections (bottom). Adapted from **Paper VI** [109].

With that, the number of detections matching a defect (true positives) could be measured, as well as the number of detections not matching a defect (false positives) and the number of defects that were not detected (false negatives). False positives were found consistently in most specimens. Their presence was partially attributed to the incorporation of redeposited spatter particles into the material, which is enabled by the layer-by-layer nature of the process where the top layers are remelted. Part of the false positive detections (Figure 28 f-g) has the same characteristics as true positive detections (Figure 28 a-e), which indicates that the spatter redeposited in this location and was subsequently fully incorporated into the bulk, not forming a defect. Part of the FP detections has a distinct appearance, as illustrated in Figure 28 h-j. In these cases, the laser exposure pattern and short scan vectors provoke the emergence of brighter regions, as previously reported in the literature [110]. The higher local intensity combined with the surrounding darker features, i.e., specimen edges and stripe overlaps, result in detections, despite the dissimilarity of these regions to the features of interest. The resulting occurrences of FP have a higher representativity in specimens manufactured with a higher global energy input. Considering all analyzed specimens, 79% of lack of fusion defects were detected with the approach proposed in **Paper VI**.

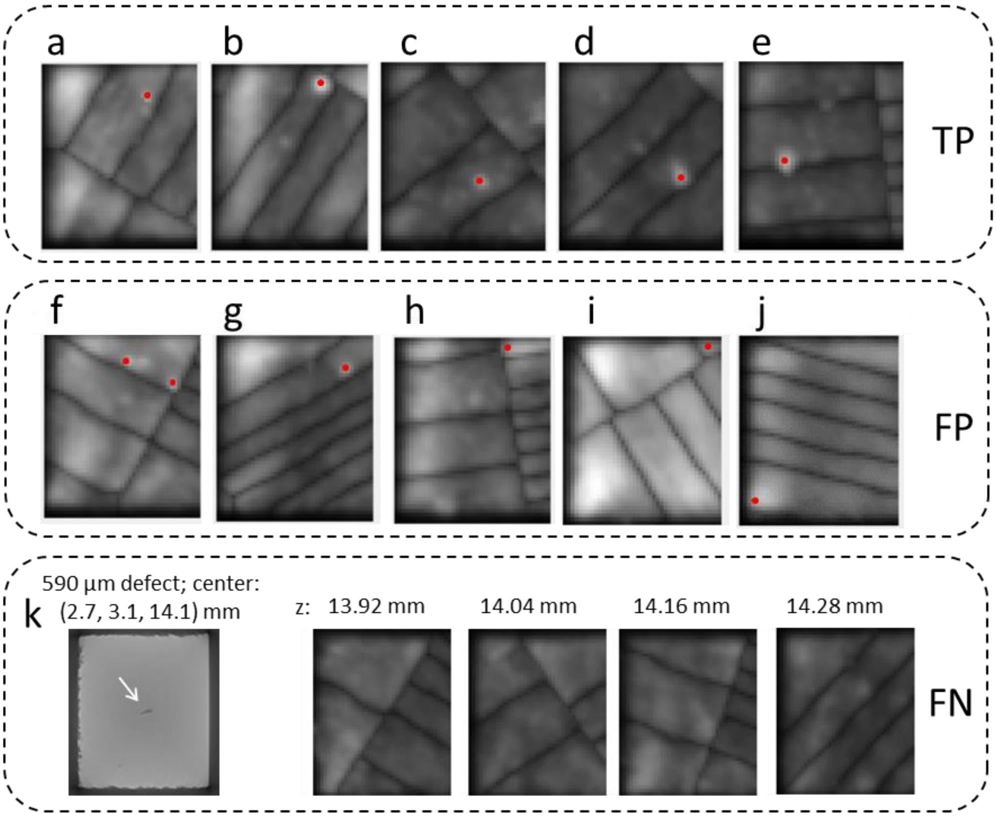
a
b
c
d
e
TP
f
g
h
i
j
FP
k
590 µm defect; center:
(2.7, 3.1, 14.1) mm
z: 13.92 mm
14.04 mm
14.16 mm
14.28 mm
FN

Figure 28: Examples of true positive (TP) occurrences (a-e), false positives (FP) (f-j), and a false negative (FN) (k). From **Paper VI**[109].

c. Impact on mechanical properties

The effect of spatter-induced lack of fusion on the mechanical properties of Hastelloy X was investigated in **Paper VIII**. Mechanical test specimens were manufactured in two builds with identical layouts (Figure 29a,c). A higher number of redeposited spatters were detected in the build where a larger nominal layer thickness was used, as observed in **Papers V, VI**, and **VII**. However, contrary to previous work, most detections were made in the central regions of the build area and toward the gas inlet instead of on the adjacencies of the gas outlet. A possible reason for this behavior is the nozzle used, which was changed from the standard EOS nozzle to the EOS grid nozzle in **Papers VIII**, **X** and **XI**.

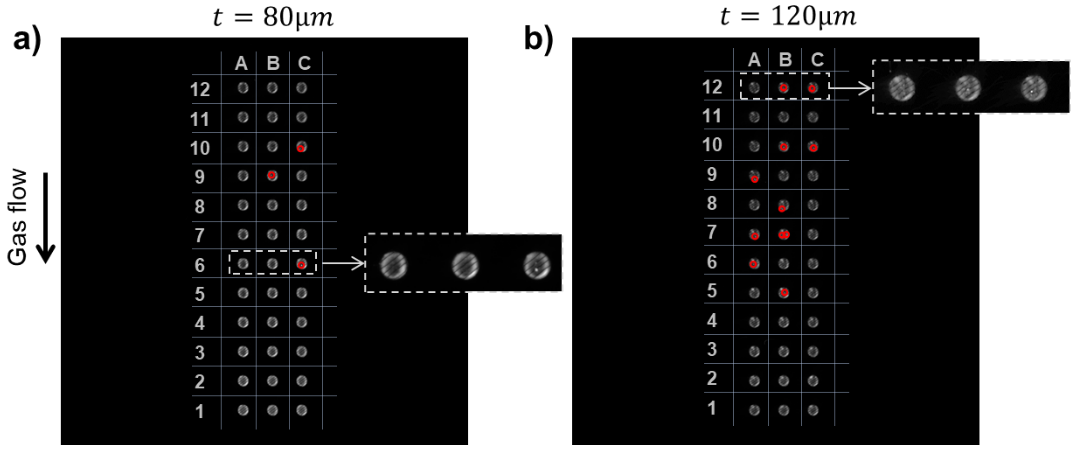
t = 80μm
t = 120μm
a)
b)
Gas flow
A
B
C
12
11
10
9
8
7
6
5
4
3
2
1

Figure 29: OT images overlayed with spatter detections (in red) show the identical build layouts used in paper VII, along with the specimen IDs, indicated by the superimposed grid. Portions of the original images are highlighted in the inserts. Adapted from **Paper VIII**.

Selected specimens were measured ex-situ using XCT to map the defect populations. Afterward, the specimens were tested in stress-controlled fatigue, and their performance was analyzed based on the measured and expected defect populations. It was confirmed that a higher build rate is associated with a higher number of lack of fusion defects. Specimens manufactured at a higher build rate presented higher scatter but significantly higher average life, despite the more critical defect population. Surprisingly, the confirmed presence of large lack of fusion defects in the gauge section of machined fatigue specimens did not necessarily result in a poorer performance of these specimens (Figure 30). It was concluded that the grain refinement obtained through the increase in nominal layer thickness has a life-prolonging effect that overrides the effects of large spatter-induced lack of fusion defects.

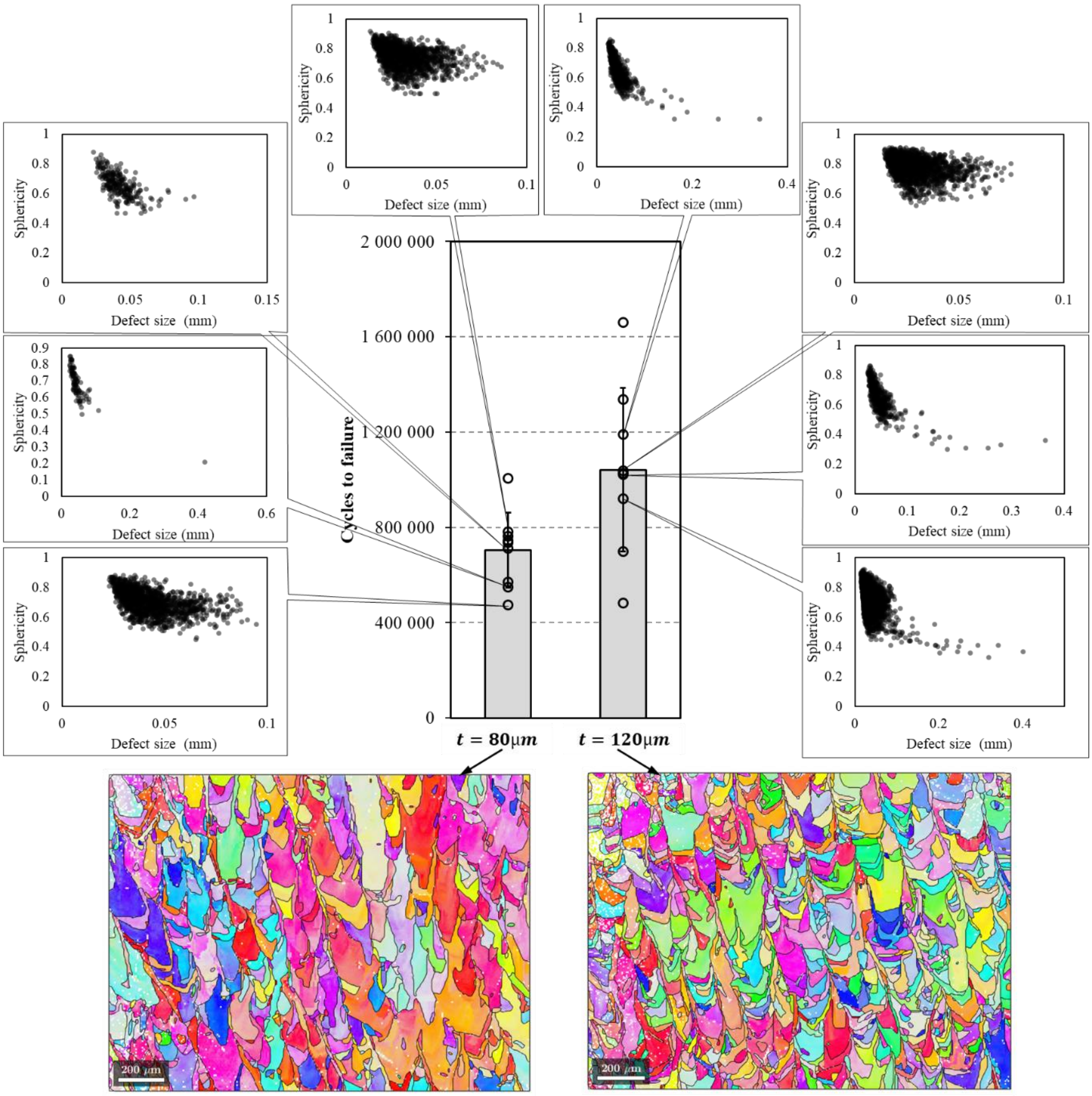

Figure 30: Defect populations in the gauge sections of different specimens, represented by defect sphericity and size. The number of cycles to failure for each of these specimens is represented, together with the performance of the remaining specimens tested in identical conditions. The error bars represent one standard deviation from the mean life in each direction. Adapted from **Paper VIII**.

d. Mitigation

Considering that spatters presumably trigger defect formation due to their oxidized surface and by hindering the laser beam energy from being completely used for melting, limiting the extent of surface oxidation could mitigate their defect-forming capabilities. **Paper IX** is a first step in that direction and investigates what characteristics of spatter particles are changed when the oxygen content in the process atmosphere is reduced from a maximum of 1000 ppm to 50 ppm. Spatter particles were collected in two locations in the build chamber, where mixing with the feedstock powder is deemed minimal. A negligible increase in the oxide thickness compared to the virgin state is observed when the oxygen content is kept under 50 ppm in the process atmosphere (Figure 31a). The surface chemical composition, however, changes, with a decrease in the Fe, Ni, Mo and Si contents and an increase in Al, Ti, and Cr contents (Figure 31b).

Point-based depth profiles in individual particles revealed an important particle-to-particle variation in terms of surface oxide thickness (Figure 32). For spatters collected from the 1000-ppm oxygen atmosphere, the measurements varied from 9.7 nm to 139.8 nm and from 2.6 nm to 36.7 nm for the 50-ppm oxygen spatters. This variability can be another reason some spatter particles are fully incorporated into the bulk while others are not, thus generating defects. The thickest surface oxides were measured in particles necessarily generated in-process, i.e., in particles larger than 63 µm, which corresponds to the sieve opening and is the maximum feedstock particle size.

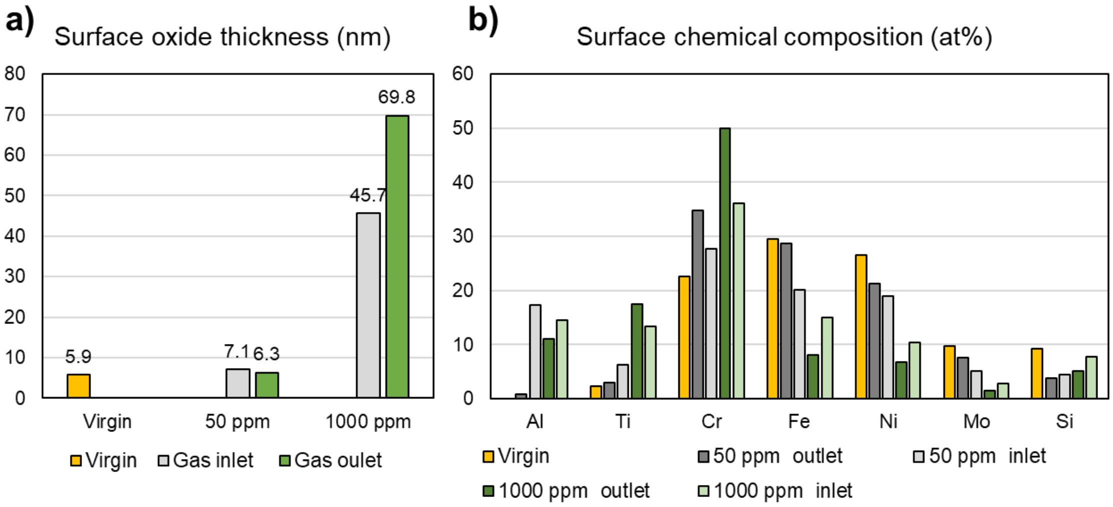

Figure 31: XPS measurements performed on the virgin powder and spatter particles. a) Surface oxide thickness; b) Surface chemical composition (not accounting for oxygen and carbon). From **Paper IX** [111].

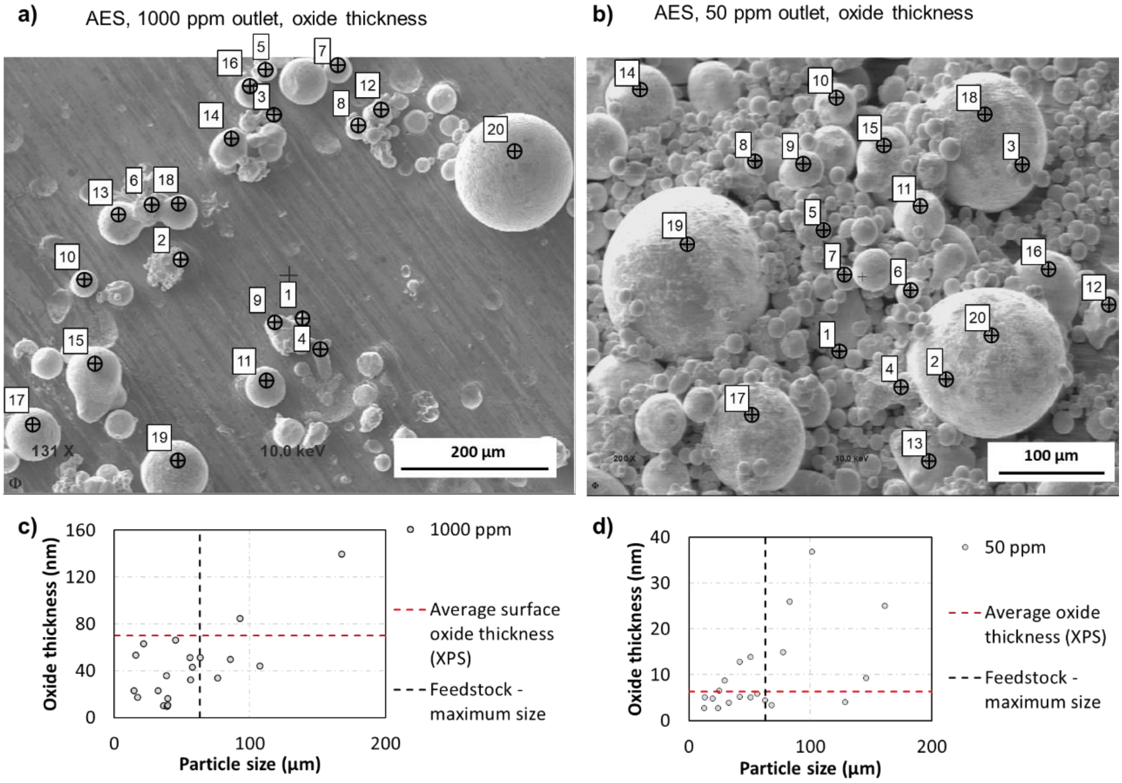

Figure 32: Oxide thickness measured in 20 different particles of (a) 1000-ppm gas outlet sample; (b) 50-ppm gas outlet sample. The measurement locations are indicated by a cross and are labeled 1 to 20. (c) and (d) show the oxide thickness plotted against the particle size for the 1000 ppm and the 50 ppm samples, respectively. From **Paper IX** [111].

To evaluate whether the restriction of the oxygen content in the process atmosphere to a maximum of 50 ppm can mitigate defect formation and improve mechanical properties, the experiments performed in **Paper VIII** were replicated under this condition in **Paper X**. While qualitative analysis of OT images highlighting spatter trajectories indicates a reduction in the formation of spatter (Figure 33), the quantitative analysis, reveals a reduction in the number of detected spatter redeposits within the gauge sections of specimens only for the nominal layer thickness of 80 µm. For 120 µm layer thickness, more spatter redeposits were detected upstream (positions 6-10 as per Figure 29) for the more controlled process atmosphere. Accordingly, in these specimens, a larger number of lack of fusion defects were measured via XCT (Figure 35). The fatigue lives in the 120 µm layer thickness group presents a large scatter, and two subgroups could be identified: a high-performing group, with few detections of spatter redeposits and with either no or few defects on the fatigue fracture surface; a poor-performing group, with a higher number of detections of spatter redeposits in OT images and internal defects in XCT. In the fracture surfaces of the latter subgroup, multiple sizeable defects were identified, and the defect formation was deemed too substantial to be countered by the material's finer microstructure. On the other hand, for 80 µm nominal layer thickness, a low number of spatter redeposits were detected in OT images, and, accordingly, a lower number of defects were measured in XCT and observed on the fatigue fracture surfaces. The tensile and fatigue performances were improved with the restriction of oxygen content in this case. Nonetheless, it could be concluded that reducing the oxygen content in the LPBF process atmosphere is not an effective strategy to mitigate stochastic defect formation.

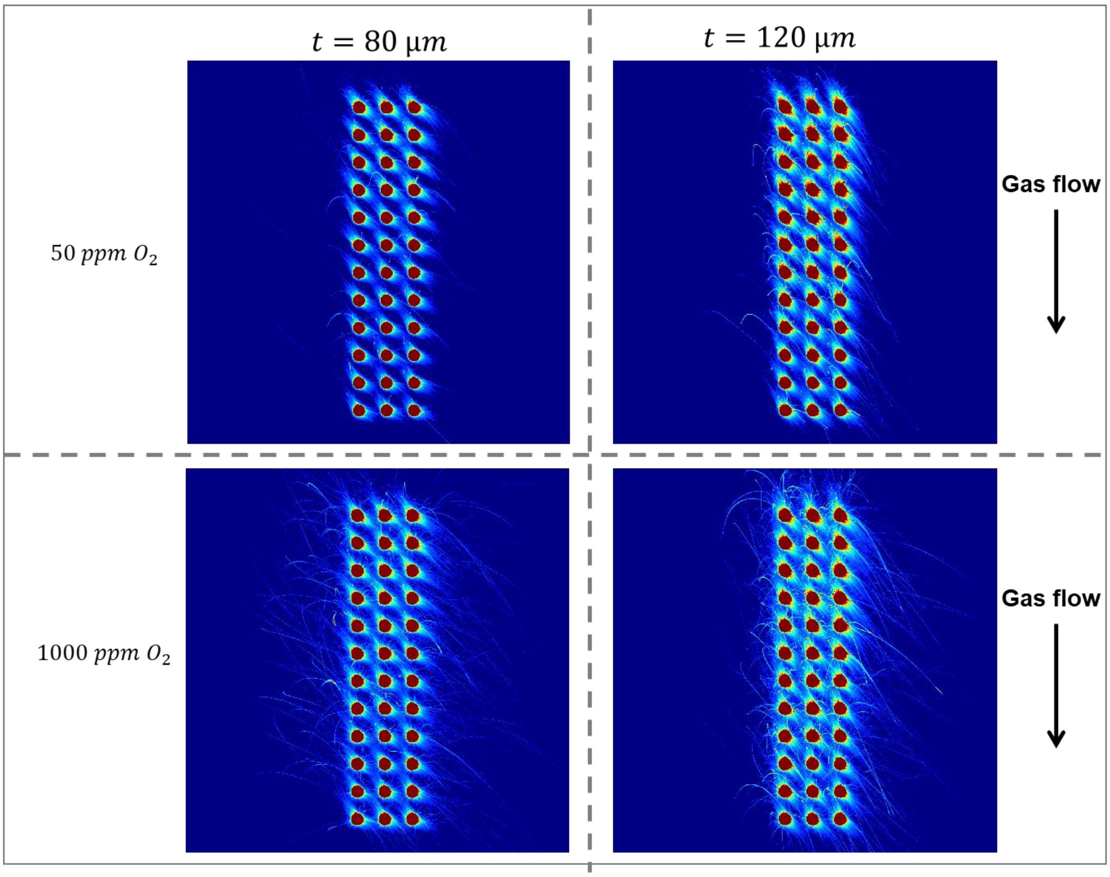

Figure 33: Qualitative OT analysis in the form of pseudocolor OT images with enhanced brightness showing spatter trajectories. Adapted from **Paper X**.

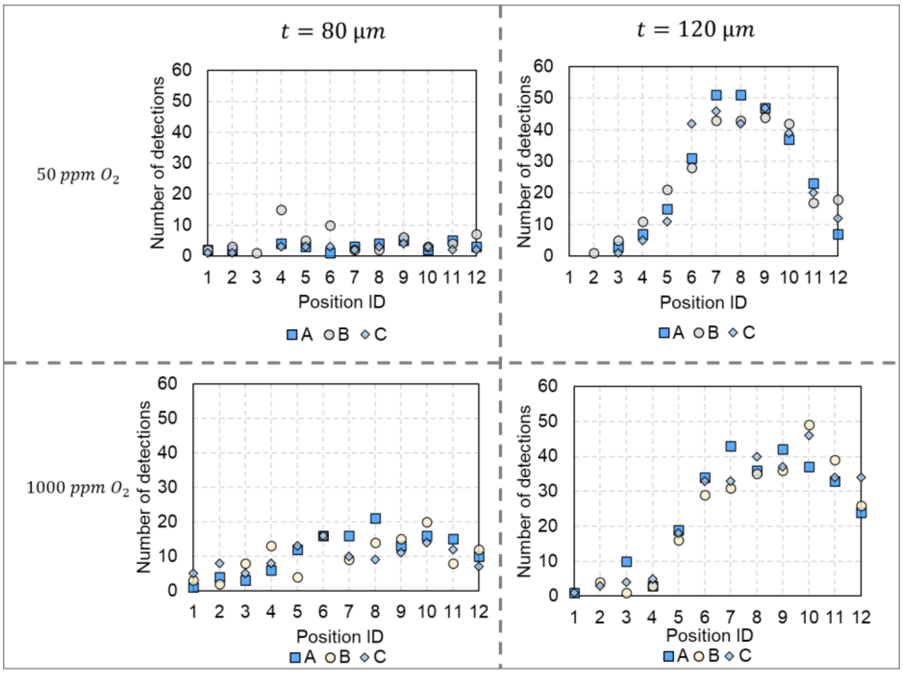

Figure 34: Quantitative OT analysis in the form of plots showing the number of spatter detections in the gauge section of each specimen. Adapted from **Paper X**.

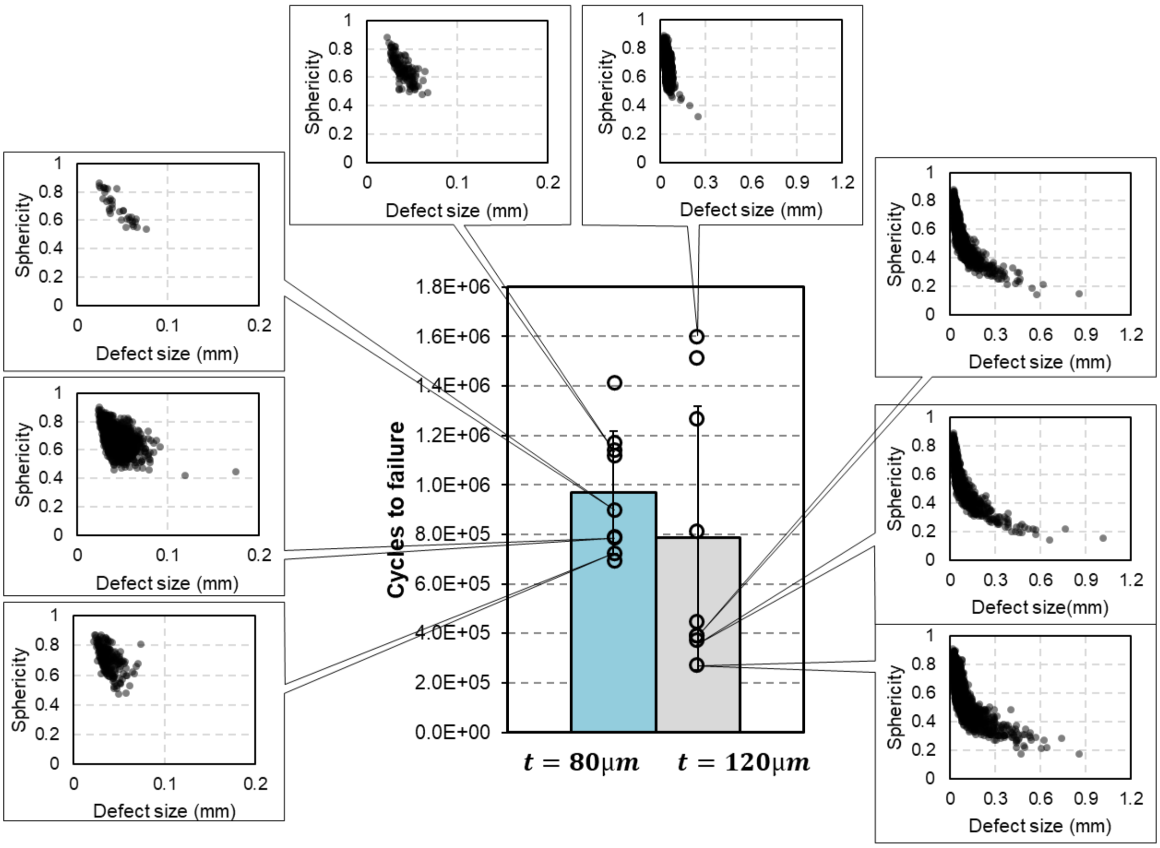

Figure 35: Fatigue performance and XCT defect data of specimens manufactured in process atmosphere with a maximum of 50 ppm oxygen. Adapted from **Paper X**.

Yet another strategy to mitigate spatter-induced defect formation was explored in **Paper XI**. A non-rotating laser scan pattern oriented perpendicularly to the direction of gas flow (Figure 36a) can potentially aid the removal of spatter particles from the build area since the particles are ejected with an initial velocity vector with no component against the gas flow direction, as shown by the OT image in Figure 36b. Nonetheless, the quantification of spatter redeposits within the gauge sections of individual specimens (Figure 36c) reveals a high number of spatter redeposits on the upper half of the build plate (upstream). Compared to a set of specimens manufactured with identical conditions but rotating scan pattern, higher average fatigue life was measured in both test stress ranges, but also a much larger scatter in data was observed (Figure 37a). The large scatter in fatigue life was attributed to the varying extensions of defect formation in the tested specimens. About half of the specimens contained a lack of fusion defect in the fracture initiation site (e.g., Figure 37c) and a significant number of spatter redeposit detections. The outliers, indicated by the arrows in Figure 37a, presented lack of fusion defects along with the scan pattern lines (Figure 37d,e), visible on the fracture surfaces of all specimens.

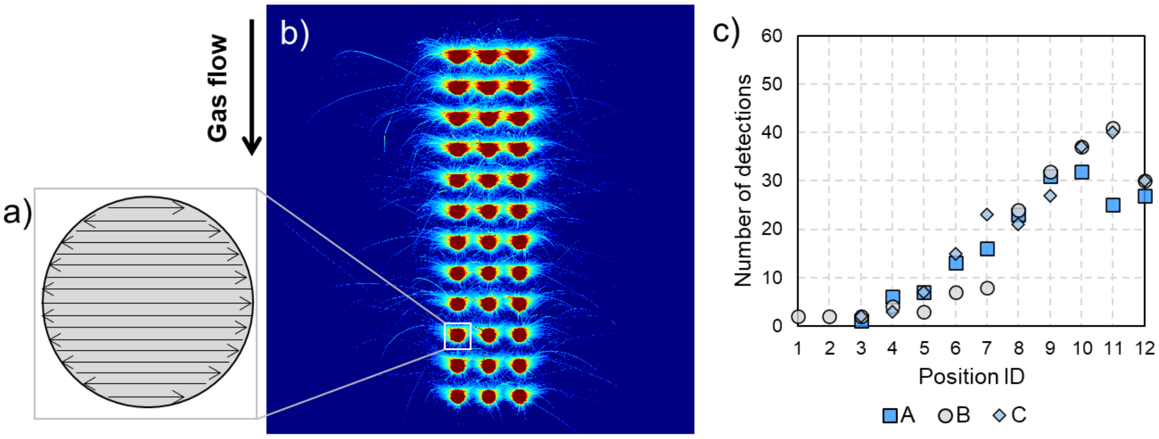

Figure 36: a) Modified laser scan pattern oriented perpendicularly to the gas flow direction. b) Pseudocolor OT images with enhanced brightness showing spatter trajectories. c) Number of spatter detections in the gauge section of each specimen. Adapted from **Paper XI**.

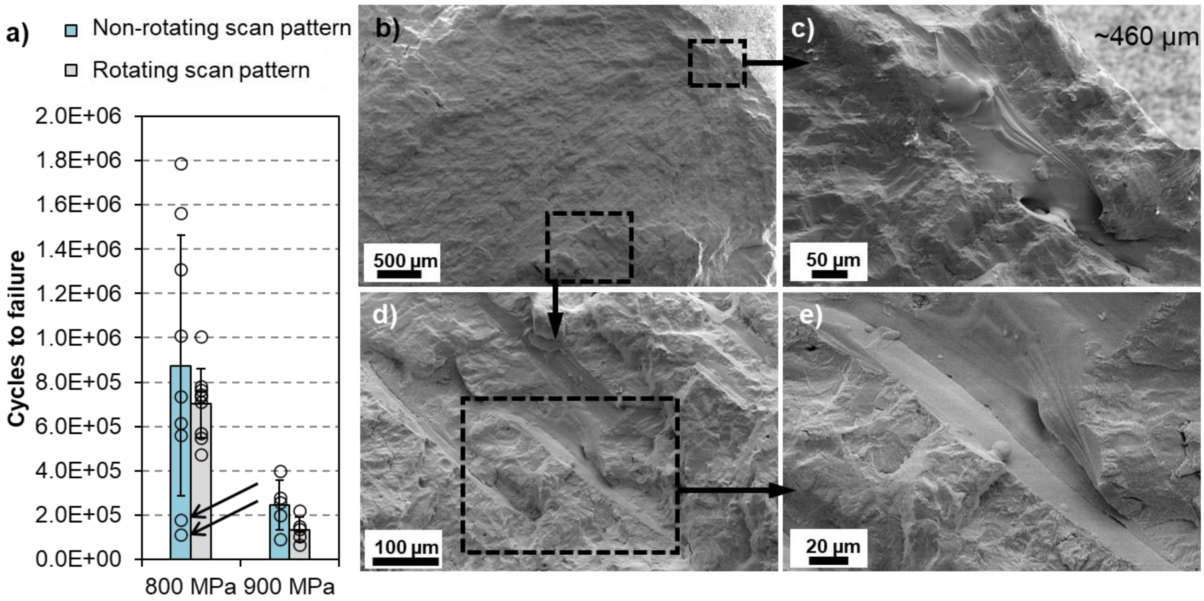

Figure 37: Fatigue life of specimens manufactured with non-rotating laser scan pattern compared to specimens manufactured in identical conditions but with rotating scan pattern (a). The fracture surface of one of the outliers indicated (b-e). Adapted from **Paper XI**.

Since the in-process defect mitigation strategies investigated proved to have limited effectiveness, the capability of hot isostatic pressing (HIP) in healing stochastic defects post-manufacturing was examined. The gauge sections of one specimen from each condition investigated in Papers VIII, X and XI were measured via XCT at Bundesanstalt für Materialforschung und -prüfung (BAM) by Dr. Tatiana Mishurova. Their defect populations can be seen in Figure 38. After HIP, no internal defects were observed in any of the specimens. All defects were apparently eliminated, despite their presumed initial oxidized surface and their large size and abundance in some of the specimens investigated. Thus, these preliminary results indicate that HIP is the most promising strategy to mitigate stochastic, spatter-induced lack of fusion.

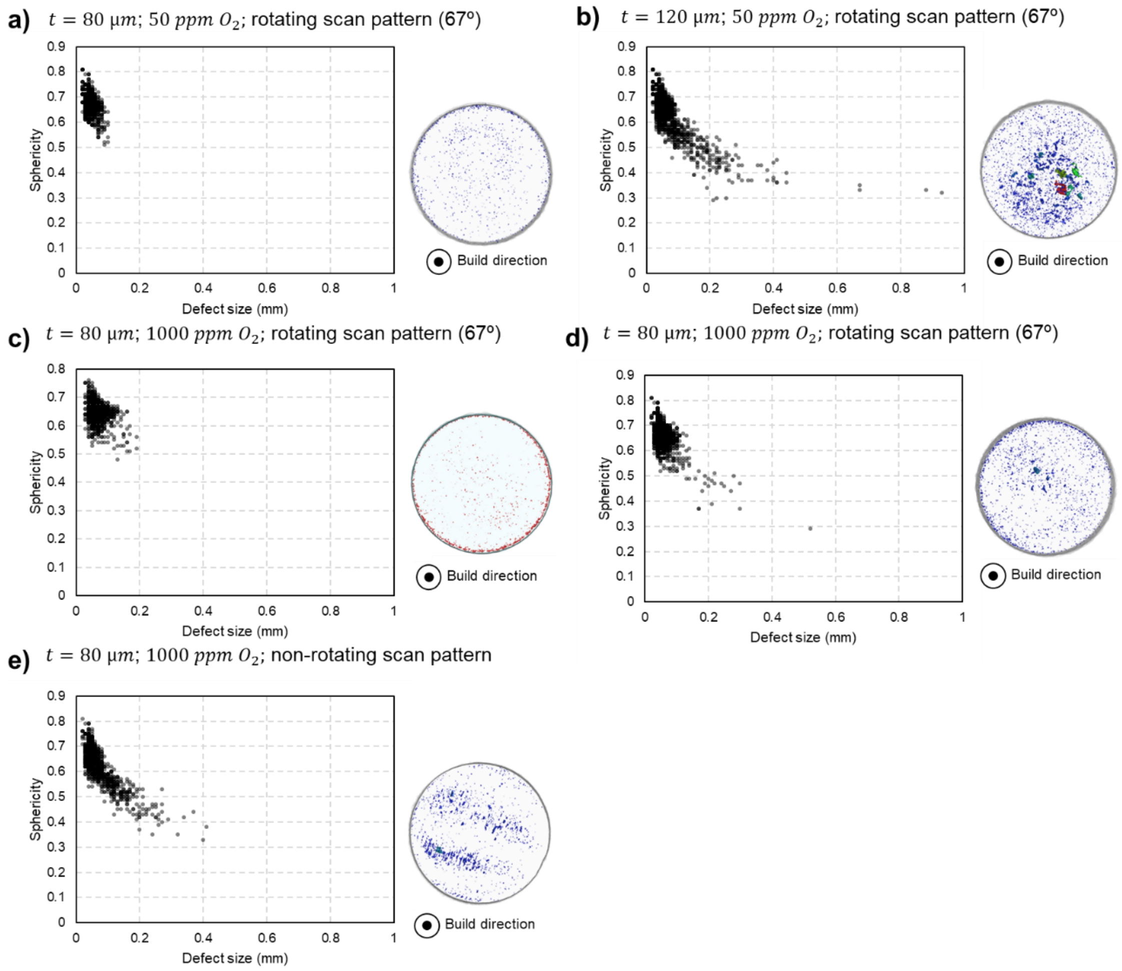
a) $t = 80\ \mu m$; $50\ ppm\ O_2$; rotating scan pattern (67°)

b) $t = 120\ \mu m$; $50\ ppm\ O_2$; rotating scan pattern (67°)

c) $t = 80\ \mu m$; $1000\ ppm\ O_2$; rotating scan pattern (67°)

d) $t = 80\ \mu m$; $1000\ ppm\ O_2$; rotating scan pattern (67°)

e) $t = 80\ \mu m$; $1000\ ppm\ O_2$; non-rotating scan pattern

Figure 38: Internal defects measured via XCT pre-HIP. No defects were measured in any of these specimens post-HIP. The variable manufacturing conditions are specified in each case (nominal layer thickness *t*, maximum allowed oxygen content in the process atmosphere, and laser scan pattern).

CHAPTER 8
CONCLUSIONS

This thesis addressed the detection of internal defects in LPBF Hastelloy X via in-situ monitoring, how the defect populations within the material change with increased process productivity, and how mechanical properties are affected by these defects. Additionally, some defect mitigation strategies were proposed and investigated. The deliberate creation of defects was performed according to two distinct approaches that preserve defect formation mechanisms in realistic manufacturing settings. Defects were created systematically in an extensive process mapping, and stochastically by boosting the amount of process by-products, while the build processes were monitored. The signal acquired through the monitoring systems was processed to identify deviations that could be coupled to defects and to melt pool features characterized ex-situ. The process mapping also set the basis for process-optimized productivity increase.

The comprehensive design of experiments performed for Hastelloy X investigated 72 processing conditions in which the defect populations and melt pool sizes were thoroughly characterized. With this, the LPBF processing of Hastelloy X could be mapped, and trends in defect formation could be established, thus enabling foreseeing defect populations in processing conditions other than the ones studied. With the melt pool monitoring and optical tomography data collected during the manufacturing of these specimens, it was possible to distinguish virtually defect-free specimens from specimens containing lack of fusion and keyhole pores. Optical tomography data were analyzed through several methods, out of which convolutional neural networks performed best. The melt pool monitoring signal characteristics could not be correlated to the internal defect populations but with melt pool dimensions and processing conditions that provide a higher instant energy input, known to generate spatter (**RQ1**).

With desirable (virtually defect-free) processing conditions identified and with parametrization of the LPBF build rate based on key process parameters, a 10-fold increase in the build rate was achievable while simultaneously avoiding defects. The main direct gain in productivity is attained by increasing the layer thickness, which also results in finer, more randomly oriented grains (**RQ2**).

In the study of stochastic defects, blob detection on optical tomography images was proposed to detect spatter particles redeposited on the powder bed, thus inferring the presence of spatter-induced lack of fusion defects. Using X-ray computed tomography data (XCT) as the ground truth, it was found that 79% of lack of fusion defects could be detected in OT images, and their positions were estimated. The detection was particularly successful for large defects (**RQ1**). Processing conditions that enable high build rates were more susceptible to spatter-driven defect formation. In particular, increased nominal layer thickness increases spatter generation per layer and simultaneously reduces the healing capability of the process, as comparatively smaller volumes of material are re-processed. These spatter particles are covered with thicker surface oxides, richer in Al and Ti. Additionally, more significant inhomogeneities were observed on the powder bed with an increased nominal layer thickness (**RQ2**).

Nonetheless, the effects of these defects on the mechanical properties of Hastelloy X were limited, partly due to the high ductility of this alloy. The finer microstructure of Hastelloy X manufactured at higher build rates enhanced its fatigue properties, despite the presence of large lack of fusion defects, which significantly affected the fatigue performance of the as-built material mainly when abundantly present. Sparse lack of fusion did not necessarily affect fatigue performance (**RQ3**).

Two strategies for mitigating stochastic defects were proposed and investigated: limiting the oxygen content in the process atmosphere to reduce oxidation of process by-products, and using a non-rotating scan pattern to aid the removal of process by-products from the build area. None of these strategies effectively reduced the defect populations homogeneously across the entire processing envelope, even though improvements in the mechanical properties were observed under specific conditions. Preliminary results indicate that even large, presumably oxidized defects can be eliminated post-process by hot isostatic pressing (HIP) (**RQ4**). The fatigue performance correlated well with the defect populations predicted by analysis of in-situ monitoring data (**RQ3**).

CHAPTER 9
FUTURE WORK

Even though a single alloy, Hastelloy X, was investigated in this thesis, the principles for defect detection are expected to be generic and transferable to other alloys. This transferability must be investigated in detail in future work.

In this thesis, mechanical testing of Hastelloy X was limited to room temperature conditions and in the as-printed state. While this can be considered a reasonable baseline for a mechanical test campaign, performing tests more representative of the operational conditions intended for this alloy would be relevant, more specifically, tests post heat treatment and at elevated temperatures. Additionally, loading directions other than the build direction should be included in a more comprehensive test campaign, given the important effect of anisotropy in LPBF material.

While it was preliminarily demonstrated that hot isostatic pressing (HIP) could eliminate spatter-induced lack of fusion, further investigation is required, including evaluating the mechanical performance post-HIP. In particular, it is recommended to investigate whether the defect mitigation offered by HIP reduces the scatter in fatigue life.

The effect of the defects studied here in the oxidation and corrosion properties of LPBF HX is an unaddressed but relevant topic due to the main application areas of the alloy being due to its excellent oxidation and corrosion resistance.

This thesis focused on the detection of internal microscopic defects. However, good potential to detect design-driven defects through in-situ monitoring has been identified and investigated by MSc students Vishal Sundar and Nikhil Belsure in their thesis *“Design-driven defects in laser powder bed fusion: correlation between in-situ monitoring data and ex-situ measurements”*, supervised by Claudia Schwerz and Mats Delin (GKN Aerospace). Further development of their work would be implementing algorithms to detect the deviations that have been coupled to defects automatically.

REFERENCES

1. MANUELA - Additive Manufacturing using Metal Pilot Line. Available at: https://manuela-project.eu/.

2. Xu, J. High-performance Nickel-based Superalloys for Additive Manufacturing. (Linköping University, 2022).

3. Tomus, D., Rometsch, P. A., Heilmaier, M. & Wu, X. Effect of minor alloying elements on crack-formation characteristics of Hastelloy-X manufactured by selective laser melting. *Additive Manufacturing* **16**, 65–72 (2017).

4. Marchese, G. *et al.* Study of the microstructure and cracking mechanisms of hastelloy X produced by laser powder bed fusion. *Materials (Basel).* **11**, (2018).

5. DebRoy, T. *et al.* Additive manufacturing of metallic components – Process, structure and properties. *Progress in Materials Science* **92**, 112–224 (2018).

6. *ASTM F2792 - 12a, Standard Terminology for Additive Manufacturing Technologies*. (ASTM International, 2012).

7. Gibson, I., Rosen, D. W. & Stucker, B. *Additive manufacturing technologies: Rapid prototyping to direct digital manufacturing*. *Additive Manufacturing Technologies: Rapid Prototyping to Direct Digital Manufacturing* (Springer US, 2010). doi:10.1007/978-1-4419-1120-9

8. Frazier, W. E. Metal additive manufacturing: A review. *Journal of Materials Engineering and Performance* **23**, 1917–1928 (2014).

9. Pakkanen, J. A. Designing for Additive Manufacturing - Product and Process Driven Design for Metals and Polymers. (2018). doi:10.6092/POLITO/PORTO/2714732

10. Klemens, P. G. Heat balance and flow conditions for electron beam and laser welding. *J. Appl. Phys.* **47**, 2165–2174 (1976).

11. Debroy, T. & David, S. A. Physical processes in fusion welding. *Rev. Mod. Phys.* **67**, (1995).

12. Metzbower, E. A. Keyhole formation. *Metall. Trans. B* **24**, 875–880 (1993).

13. Rai, R., Elmer, J. W., Palmer, T. A. & Debroy, T. Heat transfer and fluid flow during keyhole mode laser welding of tantalum, Ti-6Al-4V, 304L stainless steel and vanadium. *J. Phys. D. Appl. Phys.* **40**, 5753–5766 (2007).

14. Liu, Y., Yang, Y., Mai, S., Wang, D. & Song, C. Investigation into spatter behavior during selective laser melting of AISI 316L stainless steel powder. *Mater. Des.* **87**, 797–806 (2015).

15. Khairallah, S. A., Anderson, A. T., Rubenchik, A. & King, W. E. Laser powder-bed fusion additive manufacturing: Physics of complex melt flow and formation mechanisms of pores, spatter, and denudation zones. *Acta Mater.* **108**, 36–45 (2016).

16. Ly, S., Rubenchik, A. M., Khairallah, S. A., Guss, G. & Matthews, M. J. Metal vapor micro-jet controls material redistribution in laser powder bed fusion additive manufacturing. *Sci. Rep.* **7**, 1–12 (2017).

17. Bidare, P., Bitharas, I., Ward, R. M., Attallah, M. M. & Moore, A. J. Fluid and particle dynamics in laser powder bed fusion. *Acta Mater.* **142**, 107–120 (2018).

18. Young, Z. A. *et al.* Types of spatter and their features and formation mechanisms in laser powder bed fusion additive manufacturing process. *Addit. Manuf.* **36**, 101438 (2020).

19. Wang, D. *et al.* Mechanisms and characteristics of spatter generation in SLM processing and its effect on the properties. *Mater. Des.* **117**, 121–130 (2017).

20. Simonelli, M. *et al.* A Study on the Laser Spatter and the Oxidation Reactions During Selective Laser

Melting of 316L Stainless Steel, Al-Si10-Mg, and Ti-6Al-4V. *Metall. Mater. Trans. A Phys. Metall. Mater. Sci.* **46**, 3842–3851 (2015).

21. Esmaeilizadeh, R. *et al.* On the effect of spatter particles distribution on the quality of Hastelloy X parts made by laser powder-bed fusion additive manufacturing. *J. Manuf. Process.* **37**, 11–20 (2019).
22. Ladewig, A., Schlick, G., Fisser, M., Schulze, V. & Glatzel, U. Influence of the shielding gas flow on the removal of process by-products in the selective laser melting process. *Addit. Manuf.* **10**, 1–9 (2016).
23. Wang, D. *et al.* Influence of spatter particles contamination on densification behavior and tensile properties of CoCrW manufactured by selective laser melting. *Opt. Laser Technol.* **121**, 105678 (2020).
24. Tang, M. & Pistorius, P. C. Oxides, porosity and fatigue performance of AlSi10Mg parts produced by selective laser melting. *Int. J. Fatigue* **94**, 192–201 (2017).
25. Leung, C. L. A. *et al.* The effect of powder oxidation on defect formation in laser additive manufacturing. *Acta Mater.* **166**, 294–305 (2019).
26. Schwerz, C. *et al.* In-situ detection of redeposited spatter and its influence on the formation of internal flaws in laser powder bed fusion. *Addit. Manuf.* 102370 (2021). doi:10.1016/J.ADDMA.2021.102370
27. Ma, M., Wang, Z., Gao, M. & Zeng, X. Layer thickness dependence of performance in high-power selective laser melting of 1Cr18Ni9Ti stainless steel. *J. Mater. Process. Technol.* **215**, 142–150 (2015).
28. Sun, Z., Tan, X., Tor, S. B. & Yeong, W. Y. Selective laser melting of stainless steel 316L with low porosity and high build rates. *Mater. Des.* (2016). doi:10.1016/j.matdes.2016.05.035
29. de Formanoir, C. *et al.* Increasing the productivity of laser powder bed fusion: Influence of the hull-bulk strategy on part quality, microstructure and mechanical performance of Ti-6Al-4V. *Addit. Manuf.* **33**, (2020).
30. Attaran, M. The rise of 3-D printing: The advantages of additive manufacturing over traditional manufacturing. *Bus. Horiz.* **60**, 677–688 (2017).
31. Leicht, A., Fischer, M., Klement, U., Nyborg, L. & Hryha, E. Increasing the Productivity of Laser Powder Bed Fusion for Stainless Steel 316L through Increased Layer Thickness. *J. Mater. Eng. Perform.* **30**, 575–584 (2021).
32. Schleifenbaum, H., Diatlov, A., Hinke, C., Bültmann, J. & Voswinckel, H. Direct photonic production: Towards high speed additive manufacturing of individualized goods. *Prod. Eng.* **5**, 359–371 (2011).
33. Buchbinder, D., Schleifenbaum, H., Heidrich, S., Meiners, W. & Bültmann, J. High Power Selective Laser Melting (HP SLM) of Aluminum Parts. *Phys. Procedia* **12**, 271–278 (2011).
34. Shi, X. *et al.* Performance of high layer thickness in selective laser melting of Ti6Al4V. *Materials (Basel).* **9**, (2016).
35. Glossary of Metallurgical and Metalworking Terms. in *Metals Handbook Desk Edition* (ASM International, 1998). doi:10.31399/asm.hb.mhde2.a0005721
36. Grasso, M. & Colosimo, B. M. Process defects and in situ monitoring methods in metal powder bed fusion: A review. *Meas. Sci. Technol.* **28**, aa5c4f (2017).
37. King, W. E. *et al.* Observation of keyhole-mode laser melting in laser powder-bed fusion additive manufacturing. *J. Mater. Process. Technol.* **214**, 2915–2925 (2014).
38. Gong, H., Rafi, K., Gu, H., Starr, T. & Stucker, B. Analysis of defect generation in Ti-6Al-4V parts made using powder bed fusion additive manufacturing processes. *Addit. Manuf.* **1**, 87–98 (2014).
39. Aboulkhair, N. T., Everitt, N. M., Ashcroft, I. & Tuck, C. Reducing porosity in AlSi10Mg parts processed by selective laser melting. *Addit. Manuf.* **1**, 77–86 (2014).
40. Snow, Z., Nassar, A. R. & Reutzel, E. W. Invited Review Article: Review of the formation and impact of flaws in powder bed fusion additive manufacturing. *Additive Manufacturing* **36**, (2020).
41. Kou, S. *Welding Metallurgy*. (John Wiley & Sons, Inc., 2003). doi:10.1002/0471434027

42. Scipioni Bertoli, U., Wolfer, A. J., Matthews, M. J., Delplanque, J. P. R. & Schoenung, J. M. On the limitations of Volumetric Energy Density as a design parameter for Selective Laser Melting. *Mater. Des.* **113**, 331–340 (2017).

43. Prashanth, K. G., Scudino, S., Maity, T., Das, J. & Eckert, J. Is the energy density a reliable parameter for materials synthesis by selective laser melting? *Mater. Res. Lett.* **5**, 386–390 (2017).

44. Schwerz, C. & Nyborg, L. A neural network for identification and classification of systematic internal flaws in laser powder bed fusion. *CIRP J. Manuf. Sci. Technol.* **37**, 312–318 (2022).

45. Taheri Andani, M., Dehghani, R., Karamooz-Ravari, M. R., Mirzaeifar, R. & Ni, J. A study on the effect of energy input on spatter particles creation during selective laser melting process. *Addit. Manuf.* **20**, 33–43 (2018).

46. Qiu, C. *et al.* On the role of melt flow into the surface structure and porosity development during selective laser melting. *Acta Mater.* **96**, 72–79 (2015).

47. *ASM Handbook, Volume 11, Failure Analysis and Prevention*. **11**, (2002).

48. Beretta, S. & Romano, S. A comparison of fatigue strength sensitivity to defects for materials manufactured by AM or traditional processes. *Int. J. Fatigue* **94**, 178–191 (2017).

49. Siddique, S. *et al.* Computed tomography for characterization of fatigue performance of selective laser melted parts. *Mater. Des.* **83**, 661–669 (2015).

50. Molaei, R. *et al.* Fatigue of additive manufactured Ti-6Al-4V , Part II : The relationship between microstructure , material cyclic properties , and component performance Theory of Critical Distance. **132**, (2020).

51. Sanaei, N. & Fatemi, A. Progress in Materials Science Defects in additive manufactured metals and their effect on fatigue performance : A state-of-the-art review. *Prog. Mater. Sci.* **117**, 100724 (2021).

52. Tammas-Williams, S., Withers, P. J., Todd, I. & Prangnell, P. B. The Influence of Porosity on Fatigue Crack Initiation in Additively Manufactured Titanium Components. *Sci. Reports 2017 71* **7**, 1–13 (2017).

53. Yadollahi, A. & Shamsaei, N. Additive manufacturing of fatigue resistant materials: Challenges and opportunities. *Int. J. Fatigue* **98**, 14–31 (2017).

54. Romano, S., Brandão, A., Gumpinger, J., Gschweitl, M. & Beretta, S. Qualification of AM parts: Extreme value statistics applied to tomographic measurements. *Mater. Des.* **131**, 32–48 (2017).

55. Li, P., Warner, D. H., Fatemi, A. & Phan, N. Critical assessment of the fatigue performance of additively manufactured Ti-6Al-4V and perspective for future research. *Int. J. Fatigue* **85**, 130–143 (2016).

56. Kahlin, M., Ansell, H. & Moverare, J. J. Fatigue behaviour of notched additive manufactured Ti6Al4V with as-built surfaces. *Int. J. Fatigue* **101**, 51–60 (2017).

57. Snow, Z. *et al.* Analysis of factors affecting fatigue performance of HIP’d laser-based powder bed fusion Ti–6Al–4V coupons. *Mater. Sci. Eng. A* **864**, (2023).

58. Zhang, M. *et al.* Fatigue and fracture behaviour of laser powder bed fusion stainless steel 316L: Influence of processing parameters. *Mater. Sci. Eng. A* **703**, 251–261 (2017).

59. Yu, C. *et al.* Influence of post-processing on very high cycle fatigue resistance of Inconel 718 obtained with laser powder bed fusion. *Int. J. Fatigue* **153**, 106510 (2021).

60. Balachandramurthi, A. R., Moverare, J., Dixit, N. & Pederson, R. Influence of defects and as-built surface roughness on fatigue properties of additively manufactured Alloy 718. *Mater. Sci. Eng. A* **735**, 463–474 (2018).

61. Reed, R. C. *The Superalloys Fundamentals and Applications*. (Cambridge University Press, 2006).

62. *ASM Metals Handbook, Volume 2, Properties and Selection: Nonferrous Alloys and Special-Purpose Materials*. (ASM International, 1990). doi:10.31399/asm.hb.v02.9781627081627

63. *ASM Metals Handbook, Volume 9, Metallography and Microstructures*. (ASM International, 2004). doi:10.31399/asm.hb.v09.9781627081771

64. Haynes International. Available at: https://www.haynesintl.com/alloys/alloy-portfolio_/High-temperature-Alloys/HASTELLOY-X-alloy.

65. Han, Q. *et al.* Laser powder bed fusion of Hastelloy X: Effects of hot isostatic pressing and the hot cracking mechanism. *Mater. Sci. Eng. A* **732**, 228–239 (2018).

66. Harrison, N. J., Todd, I. & Mumtaz, K. Reduction of micro-cracking in nickel superalloys processed by Selective Laser Melting: A fundamental alloy design approach. *Acta Mater.* **94**, 59–68 (2015).

67. Sanchez-Mata, O. *et al.* Fabrication of crack-free nickel-based superalloy considered non-weldable during laser powder bed fusion. *Materials (Basel).* **11**, 1–9 (2018).

68. Sanchez-Mata, O. *et al.* Microstructure and mechanical properties at room and elevated temperature of crack-free Hastelloy X fabricated by laser powder bed fusion. *Mater. Sci. Eng. A* **780**, (2020).

69. Ni, X. *et al.* Effect of Process Parameters on the Mechanical Properties of Hastelloy X Alloy Fabricated by Selective Laser Melting. *J. Mater. Eng. Perform.* **28**, 5533–5540 (2019).

70. Childs, T. H. C., Hauser, C. & Badrossamay, M. Selective laser sintering (melting) of stainless and tool steel powders: Experiments and modelling. *Proc. Inst. Mech. Eng. Part B J. Eng. Manuf.* **219**, 339–357 (2005).

71. Wang, Y. M. *et al.* Additively manufactured hierarchical stainless steels with high strength and ductility. *Nat. Mater.* **17**, 63–70 (2018).

72. Montero-Sistiaga, M. L. *et al.* Effect of temperature on the microstructure and tensile properties of micro-crack free hastelloy X produced by selective laser melting. *Addit. Manuf.* **31**, 100995 (2020).

73. Schwerz, C., Schulz, F., Natesan, E. & Nyborg, L. Increasing productivity of laser powder bed fusion manufactured Hastelloy X through modification of process parameters. *J. Manuf. Process.* **78**, 231–241 (2022).

74. Scime, L. & Beuth, J. Anomaly detection and classification in a laser powder bed additive manufacturing process using a trained computer vision algorithm. *Addit. Manuf.* **19**, 114–126 (2018).

75. Bartlett, J. L., Jarama, A., Jones, J. & Li, X. Prediction of microstructural defects in additive manufacturing from powder bed quality using digital image correlation. *Mater. Sci. Eng. A* **794**, (2020).

76. Lu, Q. Y., Nguyen, N. V., Hum, A. J. W., Tran, T. & Wong, C. H. Identification and evaluation defects in selective laser melted 316 L stainless steel parts via in-situ monitoring and micro computed tomography. *Addit. Manuf.* **35**, 101287 (2020).

77. Gobert, C., Reutzel, E. W., Petrich, J., Nassar, A. R. & Phoha, S. Application of supervised machine learning for defect detection during metallic powder bed fusion additive manufacturing using high resolution imaging. *Addit. Manuf.* **21**, 517–528 (2018).

78. Imani, F. *et al.* Process mapping and in-process monitoring of porosity in laser powder bed fusion using layerwise optical imaging. *J. Manuf. Sci. Eng. Trans. ASME* **140**, (2018).

79. Chua, C. K., Wong, C. H. & Yeong, W. Y. Process Control and Modeling. in *Standards, Quality Control, and Measurement Sciences in 3D Printing and Additive Manufacturing* 159–179 (Elsevier, 2017). doi:10.1016/b978-0-12-813489-4.00007-6

80. Clijsters, S., Craeghs, T., Buls, S., Kempen, K. & Kruth, J. P. In situ quality control of the selective laser melting process using a high-speed, real-time melt pool monitoring system. *Int. J. Adv. Manuf. Technol.* **75**, 1089–1101 (2014).

81. Forien, J. B. *et al.* Detecting keyhole pore defects and monitoring process signatures during laser powder bed fusion: A correlation between in situ pyrometry and ex situ X-ray radiography. *Addit. Manuf.* **35**, (2020).

82. Craeghs, T., Clijsters, S., Kruth, J. P., Bechmann, F. & Ebert, M. C. Detection of Process Failures in Layerwise Laser Melting with Optical Process Monitoring. in *Physics Procedia* **39**, 753–759 (Elsevier

B.V., 2012).

83. Bisht, M., Ray, N., Verbist, F. & Coeck, S. Correlation of selective laser melting-melt pool events with the tensile properties of Ti-6Al-4V ELI processed by laser powder bed fusion. *Addit. Manuf.* **22**, 302–306 (2018).

84. Coeck, S., Bisht, M., Plas, J. & Verbist, F. Prediction of lack of fusion porosity in selective laser melting based on melt pool monitoring data. *Addit. Manuf.* **25**, 347–356 (2019).

85. Scime, L. & Beuth, J. Using machine learning to identify in-situ melt pool signatures indicative of flaw formation in a laser powder bed fusion additive manufacturing process. *Addit. Manuf.* **25**, 151–165 (2019).

86. Zhang, Y., Hong, G. S., Ye, D., Zhu, K. & Fuh, J. Y. H. Extraction and evaluation of melt pool, plume and spatter information for powder-bed fusion AM process monitoring. *Mater. Des.* **156**, 458–469 (2018).

87. Ye, D., Hong, G. S., Zhang, Y., Zhu, K. & Fuh, J. Y. H. Defect detection in selective laser melting technology by acoustic signals with deep belief networks. *Int. J. Adv. Manuf. Technol.* **96**, 2791–2801 (2018).

88. Shevchik, S. A., Kenel, C., Leinenbach, C. & Wasmer, K. Acoustic emission for in situ quality monitoring in additive manufacturing using spectral convolutional neural networks. *Addit. Manuf.* **21**, 598–604 (2018).

89. Guo, Q. *et al.* In-situ characterization and quantification of melt pool variation under constant input energy density in laser powder bed fusion additive manufacturing process. *Addit. Manuf.* **28**, 600–609 (2019).

90. Cunningham, R. *et al.* Keyhole threshold and morphology in laser melting revealed by ultrahigh-speed x-ray imaging. *Science (80-.).* **363**, 849–852 (2019).

91. Guo, Q. *et al.* Transient dynamics of powder spattering in laser powder bed fusion additive manufacturing process revealed by in-situ high-speed high-energy x-ray imaging. *Acta Mater.* **151**, 169–180 (2018).

92. Wolff, S. J. *et al.* In-situ high-speed X-ray imaging of piezo-driven directed energy deposition additive manufacturing. *Sci. Reports 2019 91* **9**, 1–14 (2019).

93. Yadroitsev, I., Krakhmalev, P. & Yadroitsava, I. Selective laser melting of Ti6Al4V alloy for biomedical applications: Temperature monitoring and microstructural evolution. *J. Alloys Compd.* **583**, 404–409 (2014).

94. Baumgartl, H., Tomas, J., Buettner, R. & Merkel, M. A deep learning-based model for defect detection in laser-powder bed fusion using in-situ thermographic monitoring. *Prog. Addit. Manuf.* **5**, 277–285 (2020).

95. Khanzadeh, M. *et al.* In-situ monitoring of melt pool images for porosity prediction in directed energy deposition processes. *IISE Trans.* **51**, 437–455 (2019).

96. Adams, B. E., Schietinger, C. W. & Kreider, K. G. Radiation Thermometry in the Semiconductor Industry. *Exp. Methods Phys. Sci.* **43**, 137–216 (2010).

97. Mitchell, J. A., Ivanoff, T. A., Dagel, D., Madison, J. D. & Jared, B. Linking pyrometry to porosity in additively manufactured metals. *Addit. Manuf.* **31**, (2020).

98. Mohr, G. *et al.* In-situ defect detection in laser powder bed fusion by using thermography and optical tomography—comparison to computed tomography. *Metals (Basel).* **10**, (2020).

99. Abdelrahman, M., Reutzel, E. W., Nassar, A. R. & Starr, T. L. Flaw detection in powder bed fusion using optical imaging. *Addit. Manuf.* **15**, 1–11 (2017).

100. Shen, H., Rometsch, P., Wu, X. & Huang, A. Influence of Gas Flow Speed on Laser Plume Attenuation and Powder Bed Particle Pickup in Laser Powder Bed Fusion. *JOM* **72**, 1039–1051 (2020).

101. 3D Printing Software EOSTATE - EOS Monitoring & Quality Assurance for Production with Additive

Manufacturing. Available at: https://www.eos.info/en/additive-manufacturing/software-3d-printing/monitoring-software#meltpool.

102. Zenzinger, G. *et al.* Process monitoring of additive manufacturing by using optical tomography. in *AIP Conference Proceedings* **1650**, 164–170 (2015).

103. Lindeberg, T. Detecting salient blob-like image structures and their scales with a scale-space primal sketch: A method for focus-of-attention. *Int. J. Comput. Vis.* **11**, 283–318 (1993).

104. Bircher, B. A., Meli, F., Küng, A. & Thalmann, R. Metrological X-ray computed tomography at sub-micrometre precision. *Euspen's 20th Int. Conf. Exhib. (Geneva, Switzerland)* 1–4 (2020).

105. Bircher, B. A., Meli, F., Küng, A. & Thalmann, R. A geometry measurement system for a dimensional cone-beam CT. *8th Conf. Ind. Comput. Tomogr. Wels, Austria (iCT 2018)* 1–7 (2018).

106. Schwerz, C. & Nyborg, L. Linking In Situ Melt Pool Monitoring to Melt Pool Size Distributions and Internal Flaws in Laser Powder Bed Fusion. *Met. 2021, Vol. 11, Page 1856* **11**, 1856 (2021).

107. Schwerz, C. & Nyborg, L. Pixel Intensity Of Near-Infrared Long-Exposure Images Acquired In-Situ As A Quality Control Tool In Laser Powder Bed Fusion Of Ni-Base Hastelloy X. *World PM 2022 Congr. Exhib.* (2022).

108. Raza, A., Schwerz, C., Pauzon, C., Nyborg, L. & Hryha, E. Effect of layer thickness on spatters oxidation of Hastelloy X alloy during powder bed fusion-laser beam processing. *Powder Technol.* **422**, 118461 (2023).

109. Schwerz, C., Bircher, B. A., Küng, A. & Nyborg, L. In-situ detection of stochastic spatter-driven lack of fusion: application of optical tomography and validation via ex-situ X-ray computed tomography. *Addit. Manuf.* 103631 (2023). doi:10.1016/J.ADDMA.2023.103631

110. Gobert, C. *et al. Conditional generative adversarial networks for in-situ layerwise additive manufacturing data*. *Solid Freeform Fabrication 2019: Proceedings of the 30th Annual International Solid Freeform Fabrication Symposium - An Additive Manufacturing Conference, SFF 2019* (2019).

111. Schwerz, C., Cao, Y. & Nyborg, L. Surface chemical analysis of spatter particles generated in laser powder bed fusion of Hastelloy X in process atmospheres with high and low oxygen content. *Surf. Interface Anal.* (2023). doi:10.1002/SIA.7202